SINGLE MOLECULE OBSERVATION OF LIVING POLYMERIZATION

A Dissertation

Presented to the Faculty of the Graduate School

of Cornell University

In Partial Fulfillment of the Requirements for the Degree of

Doctor of Philosophy

by

Kaori Kubo

May 2018

SINGLE MOLECULE OBSERVATION OF LIVING POLYMERIZATION

Kaori Kubo, Ph. D.

Cornell University 2018

This dissertation covers one topic on a study about observation of single synthetic polymer chain growth in real time.

Synthetic polymers have broad applications ranging from automobile tires and clothing due to their unique physical and chemical properties. Their properties depend not only on the characteristics of many polymer molecules collectively, but also on that of individual polymer chains. Yet, the dispersion of molecular weight is ubiquitous in synthetic polymer. Numerous studies have been conducted on controlling the molecular weight of polymers, but the origin of this dispersion under identical reaction condition has not been figured out. To answer this question, we have applied magnetic tweezers technique to synthetic polymers, and monitored the end-to-end distance of a growing polymer chain in real time upon stretching force. Surprisingly, the end-to-end distance of a growing polymer increases in a stepwise fashion, rather than increasing continually. Accordingly, we propose a 'hair-ball' forming and unraveling hypothesis during polymer growth, which is also supported by molecular dynamics simulation results. We found that the microscopic configuration of the hair-ball structure plays a key role in determining the polymerization rate of each polymer chain and in the dispersion of polymerization kinetics among individual polymers grown under identical reaction condition.

BIOGRAPHICAL SKETCH

Kaori Kubo was born in Fukuoka, Japan. She moved to Tokyo at the age of 1, where she grew up until college. She graduated from the University of Tokyo with a bachelor degree in chemistry. Her undergraduate research focused on synthesis and preparation of water-soluble fullerene vesicles. After graduation, she moved to US as a graduate student at Cornell University. She worked on observation of real-time growth of single synthetic polymer chains using magnetic tweezers, under the guidance of Professor Peng Chen. She will obtain a degree of philosophy in 2017. Outside of research, she enjoys reading, swimming, and playing tennis.

Dedicated to Maki Kubo, Keiko Hirano and Haruo Hirano

ACKNOWLEDGMENTS

I would first like to thank my advisor, Professor Peng Chen, for his guidance and help during my graduate studies. I have learned a lot from him, not only scientific knowledge but also other important things such as critical thinking skills. I also thank my committee members, Professor Michelle Wang and Professor Geoffrey Coates, for their time and valuable scientific insights.

I would like to show my gratitude to my collaborators. Professor Fernando Escobedo and Mr. Endian Wang for their work on molecular dynamics simulation and contributing to the writing of a manuscript, Dr. Angela M. DiCiccio and Dr. Rachna Khurana who helped me with synthesis.

I am also grateful for my former and current lab members. Dr. Kyu-sun Han, for initiating this project, Dr. Chunming Liu for his support in experiment, analysis and writing of this research, Dr. Feng Yang, Dr. Xiangcheng, Guanqun Chen, Ningmu Zou and all other members for their scientific discussions and friendship.

Last but not least, I would like to thank my family: my mother Maki Kubo, my grandmother Keiko Hirano, my grandfather Haruo Hirano, for always supporting and encouraging me during my entire PhD.

Table of Contents

1. Introduction

Polymerization catalysis is a key process in making synthetic polymers, which have broad applications from commodity plastics to electronics and biomedical materials (*1*-*6*). In a typical polymerization reaction, each catalyst molecule adds monomers to a growing polymer chain. These growing chains can adopt diverse conformations, which can affect the microenvironment of the catalyst, and they can also interact with one another or with themselves, leading to inter- and intra-chain reactions. Consequently, the microscopic dynamics of polymer growth is expected to differ from one polymer to another, contributing to the differences in chain length, tacticity, and co-monomer incorporation, which are crucial for their bulk properties. How a single polymer grows dynamically remains unknown, however, as polymerization dynamics has always been characterized at the ensemble level.

Here we report the first real-time visualization of polymer growth at the single-polymer level, using magnetic tweezers measurements (*7*-*10*) and focusing on the ring-opening metathesis polymerization (ROMP) catalyzed by a Grubbs' catalyst (*11*, *12*). We find that the extension of a growing polymer surprisingly does not increase continuously. Instead, it exhibits consecutive wait-and-jump steps, attributable to the formation and unraveling of conformational entanglements from newly incorporated monomers during polymerization. The features of these entanglements could be recapitulated in molecular dynamics simulations. Moreover, the microscopic configurations of these entanglements appear to play key roles in the polymerization kinetics and the kinetic dispersion among individual polymer molecules.

2. Experimental design

To visualize single-polymer growth in real time, we used magnetic tweezers (Section 5.1) (*7*-*10*) to monitor the lengthening of a polymer chain during ROMP catalyzed by the Grubbs second generation catalyst (G2, **Fig. 1A**, **B**). One end of the growing polymer is anchored to a coverslip surface via silane chemistry; the other end is connected via a C=Ru bond to the G2 catalyst, whose N-heterocyclic carbene ligand is functionalized with silane groups (**Scheme S1**) (*13*) to attach to a ~1.5 μm diameter magnetic particle (i.e., silica-coated polystyrene particle with iron oxide core; Section 5.2). A constant magnetic force (variable from 0 to ~17 pN, Section 5.1.3) pulls the particle in z direction and stretches the polymer, but is not large enough to break covalent bonds (~4 nN) (*14*, *15*). A constant force also keeps constant the ratio of the extension over contour-length of the polymer as described by the worm-like-chain (WLC) model (*16*) (Section 5.1.4). During ROMP, the insertion of new monomers into the C=Ru bond (*12*) leads to a lengthening of the extension of the polymer tether (**Fig. 1B**). By tracking the z position of the magnetic particle, we can follow the growth of a single polymer in real time with ~6-10 nm precision (Section 5.1.2). It is worth noting that our approach is distinct from an earlier atomic force microscopy study that examined surface-grafted polymers after polymerization was completed in which no real-time kinetics was obtainable (*17*).

3. Results and analysis

We first studied the growth of single polynorbornene molecules under ~17 pN at 1 M norbornene concentration in toluene, a highly solubilizing solvent for

polynorbornene (under N_2 atmosphere at room temperature, Section 5.3.1). The monomer depletion during reaction is negligible due to the high monomer-to-catalyst ratio (>10^7:1; Section 5.3.4). The G2-loaded magnetic particles were initially tethered to surface norbornene or polynorbornene via metathesis reaction, during which G2 had been initiated (*11*, *12*, *18*, *19*) and the dissociated tricyclohexylphosphine ligands (PCy_3) were washed away (Section 5.6.2). Upon monomer addition, we observed the lengthening of the polymer extension, reporting real-time polymer growth (**Fig. 1C**).

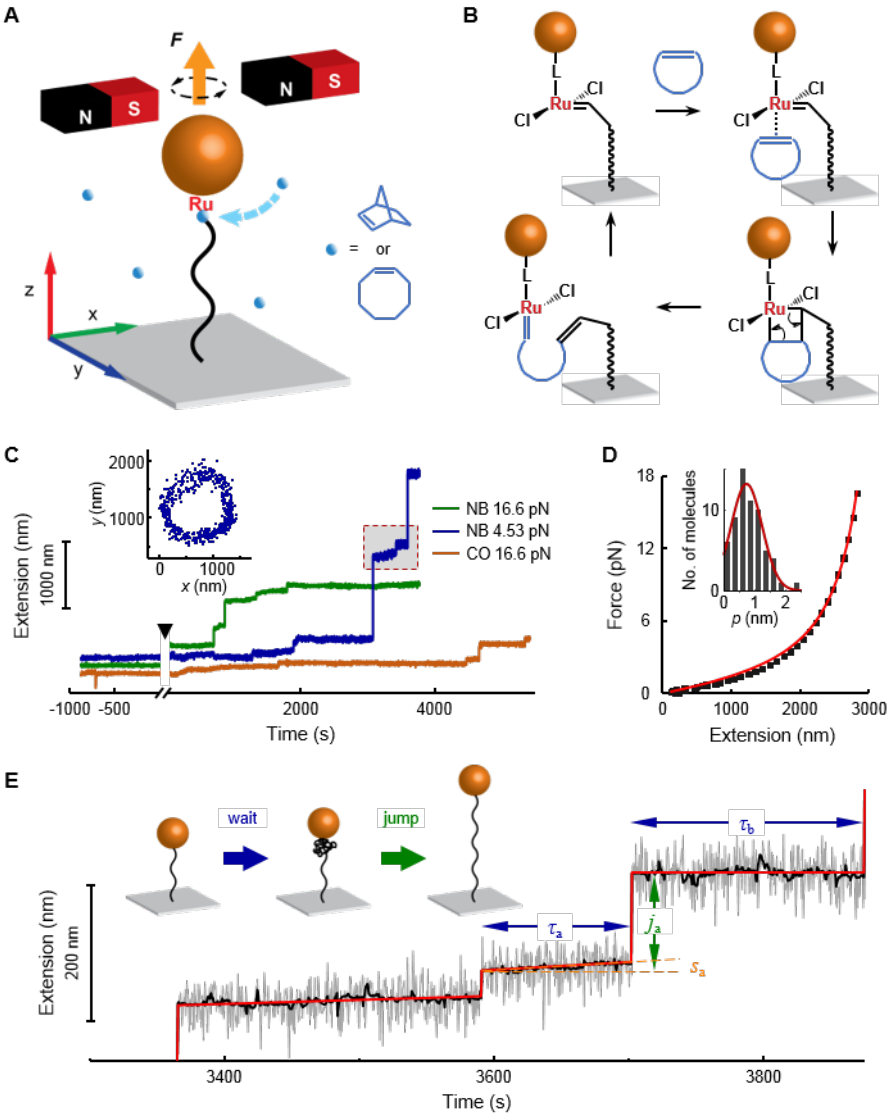

Fig. 1. Real-time visualization of single-polymer growth. (A) Schematic of magnetic tweezers measurement of a growing polymer tethered between a coverslip and a magnetic particle. Free monomers in solution (blue spheres) are incorporated into the polymer tether by the Ru-based catalyst. **(B)** General mechanism of ROMP after initiation. Each catalytic cycle inserts a new cyclic olefin monomer into the C=Ru bond of the polymer tether. L: N-heterocyclic carbene ligand attached to the particle via silane side-chains (**Scheme S1**). **(C)** Real-time extension-vs-time trajectories for three growing polymers in 1 M norbornene (NB) or *cis*-cyclooctene (CO) monomers in

toluene under different magnetic forces. Solid black triangle marks the monomer addition. Inset: xy center positions of the tethered magnetic particle of the blue trajectory when rotating the magnets at 4.5 pN after the reaction is complete. **(D)** Force-extension curve (black squares) of a single polymer (green trajectory in **C**) after polymerization is stopped. Red line: WLC model fitting. Inset: distribution of the persistence length p of single polynorbornene molecules; red line: Gaussian fit centered at 0.71 ± 0.12 nm. **(E)** Zoom-in of the boxed region in **C** (grey), with the smoothed (black) and the reconstituted trajectory after linear fitting of the waiting periods (red). Jump length j, waiting time τ, and slope s are defined here and in **Fig. S14**. Inset: schematic of hairball formation and unraveling during single-polymer growth, giving rise to the wait-and-jump steps in extension-vs-time trajectories.

Surprisingly, the extension of a single growing polymer does not increase continuously, but exhibits consecutive wait-and-jump steps (**Fig. 1C**, **E**), even though in toluene and under the applied force, polynorbornene should follow WLC behavior in which the extension scales linearly with chain length. The waiting periods are hundreds of seconds, during which the extension barely lengthens. The jumps are up to ~10^3 nm, equivalent to thousands of monomers (see extension to contour length and monomer number conversion in Section 5.1.4.2), and instantaneous within our shortest time resolution (0.05 s, **Fig. S15**). As these jumps are orders of magnitude faster than the average polymerization rate (~10^0 monomers s^{-1}; see **Fig. 3G** later), the corresponding polymer growth could not have occurred during the jump, but must have occurred during the preceding waiting period. In other words, during the waiting

periods, the newly incorporated monomers do not immediately add to the extension of the polymer, but appear "concealed" instead, perhaps in a conformationally entangled "hairball" (**Fig. 1E**, inset). With the continuing polymer growth and the applied pulling force, this hairball would eventually unravel, releasing the newly grown chain length and giving an instantaneous extension jump (**Fig. 1E**, inset).

To ensure we indeed observed single-polymer growth, we rotated the tethered magnetic particles at a pulling force under which the polymer conformation is in the aligned state (e.g., ~4.5 pN (*10*)) both before adding monomers and after stopping the reaction by flushing out monomers. Magnetic particles with single tethers exhibit characteristic free rotation and show circular precession movements in the xy plane (**Fig. 1C** inset) (*20*), whereas those with multiple tethers show irregular movements because of tether braiding (Section 5.5.2). We further measured force-extension curves of the individual polymers afterward. They follow WLC satisfactorily, with an average persistence length $p \sim 0.71$ nm (**Fig. 1D**), consistent with those of related synthetic polymers in good solvents (e.g., $p \sim 0.47$ nm for poly(ethylene glycol)) (*10*). WLC model fitting of the force-extension curve also gives the contour length L_0 of the eventual polymer (e.g., ~3618 nm in **Fig. 1D**, corresponding to ~5835 monomers; one norbornene ~0.62 nm (*21*)).

Anchoring the catalyst on the coverslip instead of the particle also gives the stepwise extensions of single-polymer growth (**Fig. S17**). After releasing the magnetic particle to allow the grown polymer to fully relax, the subsequently measured force-

extension still follows the WLC model without discrete jumps (**Fig. S18**). Both results rule out that the stepwise extension came from interactions between the polymer chain and the surfaces of coverslip or magnetic particle. Multiple experimental observations also rule out as possible reasons the chain-transfer reactions or PCy_3 ligand rebinding to the catalyst (SI Section 5.5.6.1 and 5.5.6.2). Furthermore, using cis-cyclooctene as the monomer, which produces a simple linear polyalkene, similar stepwise extensions were observed (**Fig. 1C**). Taken altogether, the stepwise extension growth, and thus the formation of the hairball, are not limited to a specific polymer and are a consequence of real-time growth under nonequilibrium, continual polymerization reaction conditions.

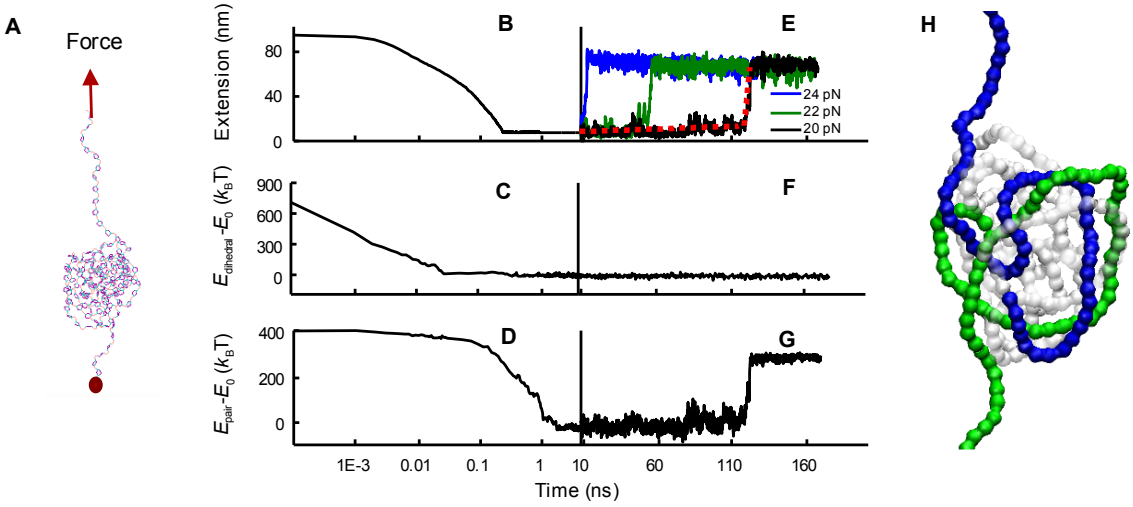

Fig. 2. Molecular dynamics simulation of hairball formation and unraveling. (A) Structure of a hairball at 2 ns from a collapsed 146-mer polynorbornene chain with one chain-end fixed and the other chain-end pulled by a constant force. **(B-D)** Time evolutions of extension **(B)**, dihedral potential **(C)**, and non-bonded pair potential **(D)** of a 146-mer polynorbornene chain collapsing from a linear configuration into a

hairball. **(E-G)** Subsequent evolutions upon applying a constant pulling force starting at 8 ns. **E** shows results from three different applied forces; red dashed lines: linear regression fits to the waiting and jumping portions of the 21 pN pulling curve. **F** and **G**: 21 pN only. **(H)** Topological structure of the entanglement in **A**.

We hypothesized that as new monomers are inserted, they do so with certain dihedral angles that introduce torsional strains in the newly grown chain, causing it to form entanglements, which are held together temporarily by intra-chain van der Waals interactions. This torsional strain is likely dissipated quickly by backbone rotations that twist the neighboring segments into entangled conformations forming a "hairball". The nonequilibrium entanglements gradually relax, aided by Brownian chain-solvent collisions and by the applied force, until the hairball unravels and subsequently behaves as a typical WLC.

We used classical molecular dynamics simulations (*22*-*28*) to test our hypothesis. To model a short chain bearing such strains, we created a polynorbornene chain with 146 monomers (~100 nm contour length) by connecting monomers randomly through the four possible configurations: *meso-cis*, *meso-trans*, *racemo-cis*, and *racemo-trans* (*29*-*31*), with the initial dihedral angles shown in **Fig. S20**-**Fig. S21**. (Four limiting cases using only one of these configurations gave similar results as those reported below.) In its starting linear-chain configuration, the two chain-ends and the initial torsional angles were fixed while both bending angles and bond lengths were allowed to relax. We then freed up one chain-end and let the polymer chain fully

relax; it spontaneously collapses into an entangled hairball (**Fig. 2A**), concurrent with a shortening of its extension and fast relaxation of its dihedral strain (**Fig. 2B**, **C**).

After equilibrating the hairball for another 2 ns with its two chain-ends fixed, we applied a constant pulling force on one end (*32-34*) and monitored the extension over time. A waiting period followed by a jump is clearly observed (**Fig. 2E**), analogous to those observed experimentally (**Fig. 1C**). The entanglements in the hairball (**Fig. 2H**) constrain and slow down the extension (the waiting period) until a point when they unravel rapidly as an extension jump; no partial unraveling was observed in simulations.

A higher pulling force expectedly shortens the waiting time for the same hairball (**Fig. 2E**). While pulling, the torsional angle energy remains unchanged (**Fig. 2F**), while the non-bonded pair contacts in the hairball formed during collapse are broken as the hairball unravels (**Fig. 2D**, **G**). After the hairball unravels, the polymer extension behavior follows the WLC model with a persistence length of ~0.67 nm (**Fig. S25B**), consistent with experiments (**Fig. 1D**).

Furthermore, we conducted simulations to mimic the experimental situation where the polymer chain consists of an unraveled, relaxed half, and a nonequilibrated half with torsional strain. Under such conditions, the hairball still forms as the chain collapses, and gives the distinctive wait-and-jump behavior upon pulling (**Fig. S27**); so do simulations on polycyclooctene (**Fig. S28**).

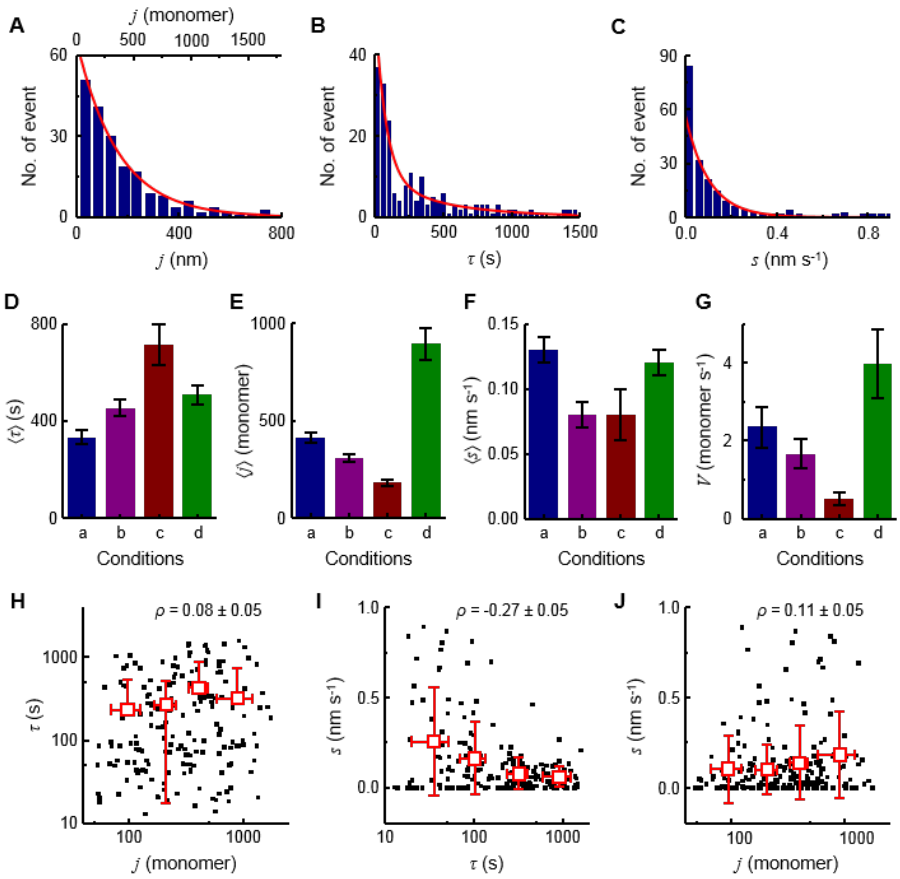

Fig. 3. Statistical properties of wait-and-jump behaviors of single-polymer growths. (A-C) Histograms of jump length j, waiting time τ, and waiting-period-slope s from 43 polymers (1 M norbornene, 17 pN force). Red lines: single **(A, C)** and double **(B)** exponential fits; the fit in **C** does not include the first bin, where s ~ 0. **(D-G)** Average waiting time $\langle\tau\rangle$, average jump length $\langle j\rangle$ ($\langle\ \rangle$ denotes averaging), average slope S, and the average polymerization rate V of individual polymers under different conditions (NB: norbornene, CO: *cis*-cyclooctene; [Olefin]: monomer concentration in molar). S of each polymer is its total extension expansion during the waiting times divided by the total waiting time; V of each polymer is its total growth length divided by the total growth time (Section 5.4). **(H-J)** Correlation plots and Pearson's correlation

coefficients between τ, j, and s from polymers grown under 1 M norbornene and 17 pN force. Each solid black square: one wait-and-jump event. Open red squares: averages from bins of equal number of events. x and y error bars are s.d. The lower halves of some of the y error bars in **H** reach to negative values and could not be plotted due to the log scale.

Having verified via modeling the key features of the hairball hypothesis, we now return to experiments to examine the statistical properties of the wait-and-jump steps in the extension-vs-time trajectories (**Fig. 1E**). The jump length j is the increase of the polymer extension after a hairball unravels, reflecting the chain length newly grown into the hairball. The individual j's follow a single exponential distribution (**Fig. 3A**). With 1 M norbornene and ~17 pN pulling force, the average jump length is 175 ± 11 nm, equivalent to 413 ± 26 monomers for an average hairball size. The waiting time τ prior to each jump is the duration of a hairball; its magnitude is thus related to the hairball's kinetic stability (it is also the period over which the hairball forms and grows during polymerization). The individual τ follows a multiexponential distribution, with at least 2 exponents (**Fig. 3B**). This multiexponential distribution suggests that either the kinetics of each hairball's unraveling (which breaks its internal non-bonded interactions) involves more than one rate-limiting step, or the individual hairballs each have different unraveling kinetics. On average, the waiting time is 333 ± 28 s, corresponding to an unravelling rate of ~0.003 s^{-1}.

Surprisingly, for the individual wait-and-jump events, the jump length j has no

significant correlation with its prior waiting time τ (Pearson's correlation coefficient $\rho_{j,\tau} = 0.08 \pm 0.05$; **Fig. 3H**), indicating that the polymer length within each hairball, as reflected by j, and the stability of the hairball, as reflected by τ, are mostly decoupled (more discussions in Section 5.7.3). This decoupling could result from the polymerization occurring locally at the catalyst center whereas the stability of the hairball is controlled by its global configuration, and the global and local configurations of a hairball may not be strongly coupled structurally.

Moreover, ~75% of the waiting periods in the extension-vs-time trajectories exhibit slightly positive slopes; the rest stays essentially flat (e.g., event a and b, respectively in **Fig. 1E**; and **Fig. 3C**). We postulate that the magnitude of slope reflects a hairball's tendency to expand during polymerization and this tendency should be related to the hairball's global "looseness". Consistently, the slope s is anti-correlated with the waiting time τ ($\rho_{s,\tau} = -0.27 \pm 0.05$; **Fig. 3I**) because a looser hairball (i.e., larger s) is expected to unravel faster (i.e., shorter τ). No significant correlation between the slope s and the jump length j is observed ($\rho_{s,j} = 0.11 \pm 0.05$; **Fig. 3J**), consistent with that the global configuration of the hairball is likely decoupled structurally from the local configuration around the catalyst center.

We then decreased the pulling force to ~4.5 pN while maintaining norbornene monomer concentration. Single-polymer growth trajectories still exhibit distinctive wait-and-jump steps (**Fig. 1C**). The average waiting time lengthens by ~53% (**Fig. 3D**); this is expected as hairball unraveling should be slower under smaller pulling

force; it is also reproduced in simulations (**Fig. 2E**). Consistently, average jump length increases by ~117% (**Fig. 3E**), as longer waiting times would allow for more polymerization reactions to occur for each hairball on average. The average slope of the waiting periods is essentially unchanged at this lower force, ~0.12 nm/s (**Fig. 3F**), which should reflect a faster hairball expansion because the same extension at a lower pulling force corresponds to a larger contour length; the faster hairball expansion here is consistent with the global hairball configuration being looser on account of a smaller pulling force. Interestingly, the average polymerization rate V increased by ~69% at this lower force (**Fig. 3G**), indicating pulling force impairs overall polymerization kinetics, perhaps via tightening the hairball to restrict access to, or distorting the structure at, the Ru center of the catalyst.

To actively manipulate ROMP activity, we decreased the norbornene monomer concentration from 1 to 0.1 M while maintaining the ~17 pN pulling force. Expectedly, the average polymerization rate of individual polymers decreases by ~29% (**Fig. 3G**). This magnitude of decrease indicates that the overall kinetics is in the sub-linear regime from 0.1 to 1 M monomer concentration, as in the classic saturation kinetics (Section 5.7.4). Consistently, the average jump length decreases by ~25% (**Fig. 3E**), reflecting smaller hairballs due to slower polymerization rates. Surprisingly, the average waiting time increases by ~36% (**Fig. 3D**), reflecting slower unraveling kinetics and more stable hairballs, even though the hairballs are smaller. We speculate that the slower polymerization rate here might allow the newly incorporated monomers to form better contacts within the hairball; consistently, the

average slope decreased by ~38% (**Fig. 3F**), reflecting tighter and more stable hairballs.

We further manipulated the ROMP activity by substituting norbornene with a less active monomer *cis*-cyclooctene (*35*). Under the same ~17 pN pulling force and 1 M monomer concentration, the average polymerization rate slows down expectedly (by ~79%; **Fig. 3G**). The average waiting time, jump length, and slope using *cis*-cyclooctene monomer all show similar trends to those using a lower norbornene concentration (**Fig. 3D-F**).

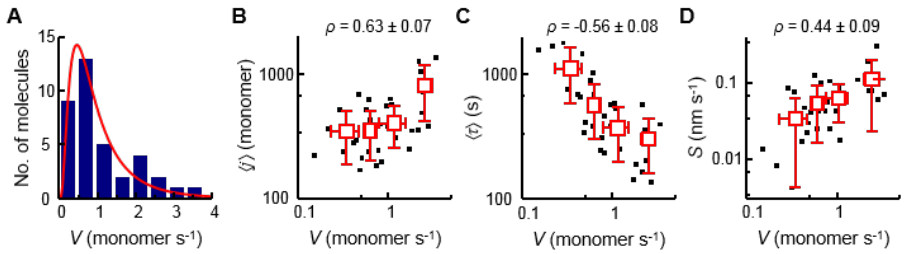

Fig. 4. Origin of kinetic dispersion in polymerization among individual polymers. **(A)** Histogram of the average polymerization rate V of individual polynorbornene molecules. Red line: lognormal fit. The polydispersity index of V is 1.5 ± 0.4. **(B-D)** Correlation plots between the average polymerization rate V of each polymer molecule and its average jump length, waiting time, and waiting-period-slope, and the respective Pearson's correlation coefficients. Each solid black square: a single polymer. Open red squares: binned and averaged results. All data here are from 1 M norbornene and 17 pN pulling force condition. x and y error bars are s.d.

With a quantitative understanding of hairball formation during real-time single-polymer growth, we examined how the microscopic properties of hairballs relate to the polymerization rate of each polymer. Under any reaction condition we studied, the polymerization rate V of individual polymers differ greatly, up to a factor of ~50 (**Fig. 4A** and **Fig. S38A**, **E**, and **I**), even though the associated polydispersity index is 1.5 ± 0.4 (Section 5.7.5), typical for ROMP (*36*). Strikingly, V of individual polymers shows strong correlations with their average jump length, waiting time, and waiting-period-slope, regardless of the reaction condition (**Fig. 4B-D** and **Fig. S38**); Pearson's cross correlation coefficients are 0.63 ± 0.07, −0.56 ± 0.08, and 0.44 ± 0.09, respectively, for 1 M norbornene at 17 pN, for example. As the jump length, waiting time, and waiting-time-slope reflect, respectively, the size, kinetic stability, and structural looseness of the hairballs that formed during each polymer's growth, these correlations indicate that faster polymerizations are associated with larger, less stable, and looser hairballs. Therefore, the microscopic configurations of the hairballs play key roles in each polymer's growth, perhaps by controlling access to the catalyst, and the dispersion of the microscopic configuration among hairballs likely contributes significantly to the dispersion of polymerization rate among individual polymers under identical growth conditions.

In typical solution synthesis of polymers, no stretching force exists and the quality of solvent could be poorer. In such conditions, conformational entangled hairballs could be more prevalent, even leading to aggregation (*10*, *37*) (Section 5.6.8), and thus play a bigger role in altering polymerization kinetics. Real-time single-

molecule visualization, as devised here, made it possible to uncover these nonequilibrium dynamic events. Novel reaction conditions, such as in a shearing solution flow, might be employed to manipulate polymer conformation to alter polymerization kinetics and potentially chain-length distribution. As biopolymer syntheses, including peptide synthesis on ribosomes, nucleic acid synthesis on polymerases, and polysaccharide synthesis in the cell wall, are also living polymerizations, it would not be unreasonable to conjecture that such nonequilibrium conformational entanglements are relevant there as well.

4. References

1. R. H. Grubbs, W. Tumas, Polymer synthesis and organotransition metal chemistry. *Science* **243**, 907-915 (1989).
2. F. Svec, J. M. Frechet, New designs of macroporous polymers and supports: From separation to biocatalysis. *Science* **273**, 205-211 (1996).
3. R. K. O'Reilly, C. J. Hawker, K. L. Wooley, Cross-linked block copolymer micelles: Functional nanostructures of great potential and versatility. *Chem. Soc. Rev* **35**, 1068-1083 (2006).
4. Z. Chen *et al*., A design principle of polymers processable into 2d homeotropic order. *Nat. Commun.* **7**, 13640 (2006).
5. J. J. Green, J. H. Elisseeff, Mimicking biological functionality with polymers for biomedical applications. *Nature* **540**, 386-394 (2016).
6. A.Rose, Z. Zhu, C. F. Madigan, T. M. Swager, V. Bulovic, Sensitivity gains in chemosensing by lasing action in organic polymers. *Nature* **434**, 876-879

(2005).

7. T. R. Strick, J. F. Allemand, D. Bensimon, A. Bensimon, V. Croquette, The elasticity of a single supercoiled DNA molecule. *Science* **271**, 1835-1837 (1996).

8. D. A. Koster, K. Palle, E. S. Bot, M. A. Bjornsti, N. H. Dekker, Antitumour drugs impede DNA uncoiling by topoisomerase i. *Nature* **448**, 213-217 (2007).

9. K. C. Neuman, A. Nagy, Single-molecule force spectroscopy: Optical tweezers, magnetic tweezers and atomic force microscopy. *Nat. Meth.* **5**, 491-505 (2008).

10. A. Dittmore, D. B. McIntosh, S. Halliday, O. A. Saleh, Single-molecule elasticity measurements of the onset of excluded volume in poly(ethylene glycol). *Phys. Rev. Lett.* **107**, 148301 (2011).

11. C. W. Bielawski, R. H. Grubbs, Living ring-opening metathesis polymerization. *Prog. Polym. Sci.* **32**, 1-29 (2007).

12. M. S. Sanford, J. A. Love, R. H. Grubbs, Mechanism and activity of ruthenium olefin metathesis catalysts. *J. Am. Chem. Soc.* **123**, 6543-6554 (2001).

13. J. Elbert *et al.*, Reversible activity modulation of surface-attached Grubbs second generation type catalysts using redox-responsive polymers. *Macromolecules* **46**, 4255-4267 (2013).

14. M. Grandbois, M. Beyer, M. Rief, H. Clausen-Schaumann, H. E. Gaub, How strong is a covalent bond? *Science* **283**, 1727-1730 (1999).

15. H. M. Klukovich, T. B. Kouznetsova, Z. S. Kean, J. M. Lenhardt, S. L. Craig, A backbone lever-arm effect enhances polymer mechanochemistry. *Nat. Chem.*

5, 110-114 (2013).

16. C. Bouchiat *et al.*, Estimating the persistence length of a worm-like chain molecule from force-extension measurements. *Biophys. J.* **76**, 409-413 (1999).
17. T. Tischer *et al*., Direct mapping of raft controlled macromolecular growth on surfaces via single molecule force spectroscopy. *ACS Macro Lett*. **5**, 498-503 (2016).
18. J. D. Ng *et al*., Single-molecule investigation of initiation dynamics of an organometallic catalyst. *J. Am. Chem. Soc*. **138**, 3876-3883 (2016).
19. A. Piermattei, S. Karthikeyan, R. P. Sijbesma, Activating catalysts with mechanical force. *Nat. Chem*. **1**, 133-137 (2009).
20. J. Lipfert, J. W. J. Kerssemakers, T. Jager, N. H. Dekker, Magnetic torque tweezers: Measuring torsional stiffness in DNA and reca-DNA filaments. *Nat. Meth*. **7**, 977-980 (2010).
21. L.-B. W. Lee, R. A. Register, Hydrogenated ring-opened polynorbornene: A highly crystalline atactic polymer. *Macromolecules* **38**, 1216-1222 (2005).
22. D. Frenkel, B. Smit, *Understanding molecular simulation: From algorithms to applications.* (Academic press, 2001).
23. V. Ganesan, A. Jayaraman, Theory and simulation studies of effective interactions, phase behavior and morphology in polymer nanocomposites. *Soft Matter* **10**, 13-38 (2014).
24. B. Dünweg, W. Paul, Brownian dynamics simulations without Gaussian random numbers. *Int. J. Mod. Phys. A* **2**, 817-827 (1991).
25. N. Grønbech-Jensen, O. Farago, A simple and effective Verlet-type algorithm

for simulating Langevin dynamics. *Mol. Phys.* **111**, 983-991 (2013).

26. N. Grønbech-Jensen, N. R. Hayre, O. Farago, Application of the G-JF discrete-time thermostat for fast and accurate molecular simulations. *Comput. Phys. Commun.* **185**, 524-527 (2014).

27. S. Plimpton, Fast parallel algorithms for short-range molecular dynamics. *J. Comput. Phys.* **117**, 1-19 (1995).

28. C. D. Wick, M. G. Martin, J. I. Siepmann, Transferable potentials for phase equilibria. 4. United-atom description of linear and branched alkenes and alkylbenzenes. *J. Phys. Chem. B* **104**, 8008-8016 (2000).

29. G. Floros *et al.*, Ring opening metathesis polymerization of norbornene and derivatives by the triply bonded ditungsten complex Na [W2 (μ-Cl) 3Cl4 (THF) 2]·(THF) 3. *Polymers* **4**, 1657-1673 (2012).

30. S. A. Gonsales *et al.*, Highly tactic cyclic polynorbornene: stereoselective ring expansion metathesis polymerization of norbornene catalyzed by a new tethered tungsten-alkylidene catalyst. *J. Am. Chem. Soc.* **138**, 4996-4999 (2016).

31. L. E. Rosebrugh, V. M. Marx, B. K. Keitz, R. H. Grubbs, Synthesis of highly cis, syndiotactic polymers via ring-opening metathesis polymerization using ruthenium metathesis catalysts. *J. Am. Chem. Soc.* **135**, 10032-10035 (2013).

32. S. Izrailev *et al.*, *Steered molecular dynamics. Computational molecular dynamics: challenges, methods, ideas*. (Springer, 1999), pp. 39-65.

33. C. Jarzynski, Nonequilibrium equality for free energy differences. *Phys. Rev. Lett.* **78**, 2690 (1997).

34. S. Park, K. Schulten, Calculating potentials of mean force from steered molecular dynamics simulations. *J. Chem. Phys.* **120**, 5946-5961 (2004).

35. P. v. R. Schleyer, J. E. Williams, K. R. Blanchard, Evaluation of strain in hydrocarbons. The strain in adamantane and its origin. *J. Am. Chem. Soc.* **92**, 2377-2386 (1970).

36. C. W. Bielawski, R. H. Grubbs, Highly efficient ring-opening metathesis polymerization (romp) using new ruthenium catalysts containing n-heterocyclic carbene ligands. *Angew. Chem. Int. Ed.* **39**, 2903-2906 (2000).

37. E. M. Hensle, S. A. Blum, Phase separation polymerization of dicyclopentadiene characterized by in operando fluorescence microscopy. *J. Am. Chem. Soc.* **135**, 12324-12328 (2013).

5. Supporting information

5.1. Instrumentation

5.1.1. Magnetic tweezers

The magnetic tweezers apparatus was built following the design of Neuman et al (38), and mounted on top of a Olympus IX71 inverted microscopy (**Fig. S1A**), which sits on a laser table (Newport, M-RS2000-46-8) with vibration isolators (Newport, S-2000 series).

Two rectangular magnets (Pacific PAC Technologies, magnetic energy density (N) = 52; NdFeBr; Ni-plated; 5×8×3 mm) are placed in a horizontal configuration with a 0.8 mm gap (**Fig. S1C**) to exert magnetic force (39). The magnets are fixed on an aluminum magnet holder (custom-made), which is connected to an aluminum plate (custom-made) via a steel tube (McMaster-Carr, 89895K421) and a ball bearing (McMaster-Carr, 6455K52) (**Fig. S1B**). The aluminum plate is attached to a *xyz* micro-stage set (Newport, 423 series), which controls the movement of the magnets in three dimensions with micrometer accuracy (**Fig. S1A**, **B**). The rotational movement of the magnets is controlled by the motor (Physik Instrumente, C-150.PD) mounted on the same aluminum plate. The rotor motor is connected with the steel tube via pulleys (McMaster-Carr, 57105K14) and a timing belt (McMaster-Carr, 1679K17) (**Fig. S1B**).

The sample flow cell is taped on top of a piezo stage (Physik Instrumente, P-527.3CL) that is mounted on the microscope stage. The piezo stage, controlled by digital piezo controller (Physik Instrumente, E710.4CL) and PI NanoCapture 3.4.0 software, is capable of moving the flow cell in three dimensions with nanometer accuracy, and is used to measure the calibration curve of *z* position.

Illumination is provided by collimated LED light (Thorlabs, LED505) mounted on the condenser holder of the microscope (**Fig. S1A**). The illumination can reach the sample by passing through the steel tube and the gap between the magnets. A 60× oil-immersion objective (OLYMPUS UPLANFL N 60X) is used for bright field transmission imaging. And the transmission images are recorded by a CCD camera (Allied Vision Prosilica GE680) with 1 ms exposure time and auto gain, controlled by GigE Vision board with vision acquisition (NI PCIe-8231) and home-written Labview software.

The rotational axis of the magnets and optical axis of the microscope are aligned by adjusting the position of magnets in the *xy* plane using the *xyz* micro-stage set while rotating the magnets (*x, y, z* directions are as defined in **Fig. S1A**). The alignment is achieved when the rotation of the magnets does not affect the brightness of the recorded transmission image.

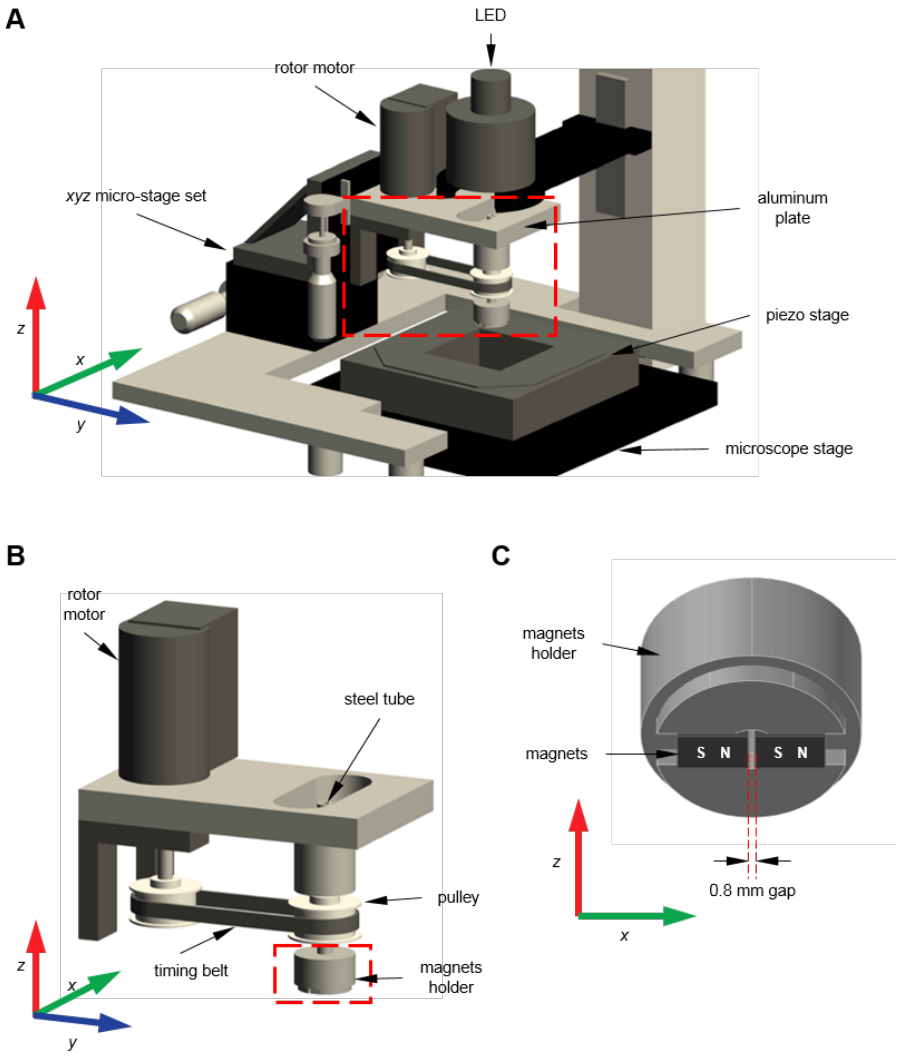

Fig. S1. Magnetic tweezers apparatus. (A) The overall diagram of magnetic tweezers apparatus built on top of an inverted optical microscope. **(B)** Zoom-in of the parts inside the red box in **A**. **(C)** Zoom-in of the parts inside the red box in **B**.

5.1.2. 3D center position tracking with nanometer precision

The *xyz* center position of a magnetic particle is determined by analyzing the bright field transmission images of the magnetic particle using custom-written Matlab script, adapting the procedures by Croquette (*40*), Dekker (*41*) and Neuman (*38*).

5.1.3. xy center position tracking with ~3nm precision

The *x* (*y*) center position is calculated by fitting the line intensity profile through the estimated center position of the particle in *x* (*y*) direction separately. The detailed procedure is as follows:

(1) Flatten the background of the transmission image by Gaussian filtering (**Fig. S2A-D**). The original transmission image (**Fig. S2A**) was first convolved with a low-pass Gaussian kernel (11×11, σ = 1 pixel) to generate a slightly smoothed image (**Fig. S2B**). The smoothed image is then treated with a boxcar kernel (11×11, pixel value = 1/121) to obtain the non-uniform background image (**Fig. S2C**). Finally, the background image is subtracted from the original image to give the background-flattened image (**Fig. S2D**) (*42*). Note the background image in **Fig. S2C** still contains some particle features, but not much their diffraction ring patterns, and after the subtraction, the diffraction ring patterns are enhanced (**Fig. S2D**). As this background subtraction approach is systematically applied to all images at different z positions, it does not affect the relative z positions that are calibrated by piezo state movements.

(2) In the first image of an image stack, the initial-guess of the *xy* center position of a particle is visually determined; and in the following images, the *xy* center position of the particle in the previous image is used as the initial-guess of *xy*

center position. And a square area of the particle (usually 61 × 61 pixel^2 square) centered at the initial-guess of the *xy* center position is extracted out (**Fig. S2E**). Then the approximate *xy* center position is obtained by applying imfindcircles Matlab function to the square image. The approximate *xy* center position will be used as the initial input value for center position fitting in step (4).

(3) Artificially enlarge the square image by 100 times (10 times on each dimension), so the new pixel size is 1/10 of the original one (**Fig. S2E**). And the coordinates of the approximate *xy* center position is also enlarged by 10 times (in units of pixels).

(4) On *x* (*y*) direction, extract the line intensity profile through the estimated center position, with a width of 5 new pixels, and fit the line scan by the following equation (**Fig. S2F**), following Dekker and coworkers (*41*):

$$I(x) = exp\left(-\frac{|x-c|}{r}\right) sin\,(-\frac{|x-c|}{\lambda} + p) \qquad \textbf{Eqn. S1}$$

Here $I(x)$ is the intensity at pixel x; x is the index of pixel along the x direction; c is the center position of the line intensity profile in the unit of pixels, which is further converted to nanometers by multiplying the new pixel size (12.3 nm); r, λ and p are floating parameters The same procedure is used along the *y* direction.

The accuracy of *x* (*y*) center position tracking is demonstrated by moving the sample along *x* (*y*) direction with 50 nm step size, controlled by the piezo stage. As shown in **Fig. S2G**, the fitted *x* (*y*) center positions of the particles follow reliably the expected trajectory. The uncertainty of *x* (*y*) position is obtained by subtracting the expected trajectory from the determined trajectory of the particles, and is ~2.6 nm, based

on Gaussian fitting of the distribution of relative x (y) center position using our image analysis procedure (**Fig. S2H**).

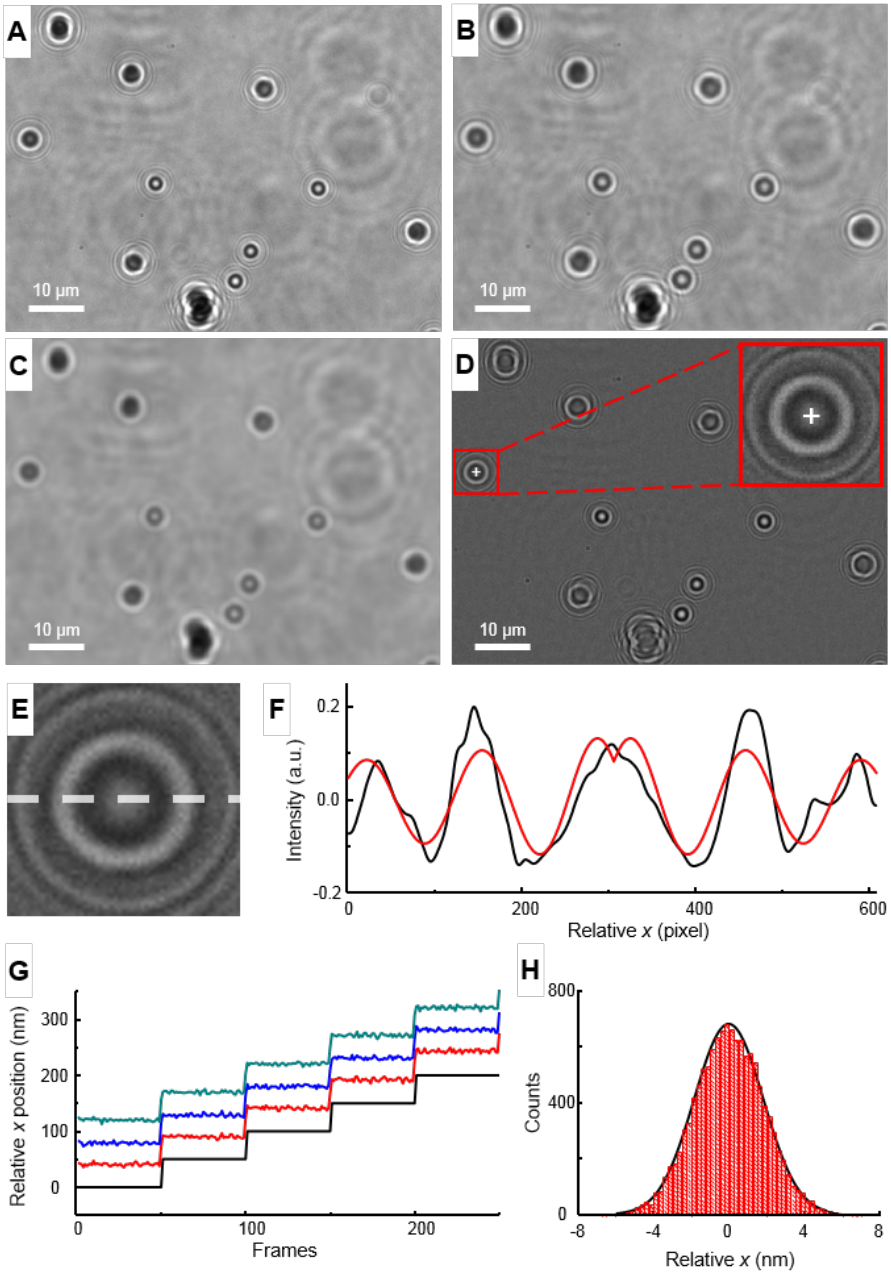

Fig. S2. Determination of *xy* center position of a particle. (A) Bright-field transmission image of magnetic particles in a flow cell. **(B)** Convolution of A with a low-pass Gaussian kernel (11×11, σ = 1 pixel). **(C)** Background image generated by

treating B with a boxcar kernel (11×11, pixel value = 1/121). **(D)** Transmission image after background subtraction. The bead in the red square is tracked, and the white cross is the estimated *xy* center position. **(E)** 100-time enlarged image of the particle in D. **(F)** The line intensity profile of the white dashed line in E (black), and the fitting of the line intensity profile using **Eqn. S1** (red). **(G)** Trajectories of particles moving on *x* direction, with 50 nm step size controlled by piezo stage. Black line is the expected trajectory; green, blue and red trajectories are the movements of three different particles. **(H)** The histogram of determined *x* center position relative to the expected *x* position. The black curve is a Gaussian fit of the histogram, with s.d. of 2.6 nm.

5.1.4. z center position tracking with ~6 nm precision

The *z* center position is calculated based on the radial intensity profile around determined *xy* center position, following Croquette and coworkers (*40*). The detailed procedure is as follows:

(1) Generate the radially averaged radial intensity profile of a particle in each image frame. First, 72 equally spaced points are generated on a circle with a certain radius (in whole integers of pixels, from 0 to the maximum radius, which is ~300) centered at the *xy* center position determined earlier (**Fig. S3A**, left). Then, the coordinates of the 72 points are rounded to integer pixels. The averaged intensity at that radius is the average of the intensities of the 72 points around the circle. Repeat this process for each radius to generate the radial intensity profile (**Fig. S3A**, right)

(2) Measure the *z* calibration map of radial intensity profiles for *each* particle that will be monitored. To do this, the sample is moved in *z* direction with 200 nm step size for a total of 8 μm controlled by the piezo stage. At each *z* position, 100 image frames are recorded at 200 Hz sampling rate with 1 ms exposure time. The calibration radial intensity profile of a particle at each *z* position is obtained by averaging the radial intensity profiles over the 100 frames. (**Fig. S3B**) During *z* calibration map measurement, ~14.5 pN magnetic force is applied to minimize the fluctuation of the tethered magnetic particles in *z* direction.

(3) Subtract the radial intensity profile of a particle at a certain *z* position from each row of its *z* calibration map (**Fig. S3C**). In this difference map, the row that has the smallest standard deviation is the approximate *z* position of the particle in 200 nm precision (**Fig. S3C**, right).

(4) To get *z* position in nanometer precision, we artificially interpolate the *z* calibration map near the approximate *z* position by 200 times, applying cubic interpolation method (**Fig. S3D**). Then repeat step (3), we can get the *z* value in nanometer precision (**Fig. S3E**).

(5) Finally, the calculated *z* position is scaled by the refractive index of solvent, $n_{solvent}$, to give the actual *z* position, as done previously (*38*).

$$z_{actual} = z_{calculated} \times n_{solvent} / n_{oil} \qquad \textbf{Eqn. S2}$$

Here n_{oil} = 1.515, $n_{solvent}$ = 1.333 for water, and 1.497 for toluene.

The accuracy of *z* center position tracking will be demonstrated in the following by measuring the length of a 5 kbp DNA. The precision of *z* measurement is 5.7 nm, determined by the fluctuations of the *z* position of position markers (**Fig. S3F**).

Additionally, the drift of sample is corrected for by tracking the position markers (i.e., polystyrene magnetic particle) that are fixed on the glass coverslip.

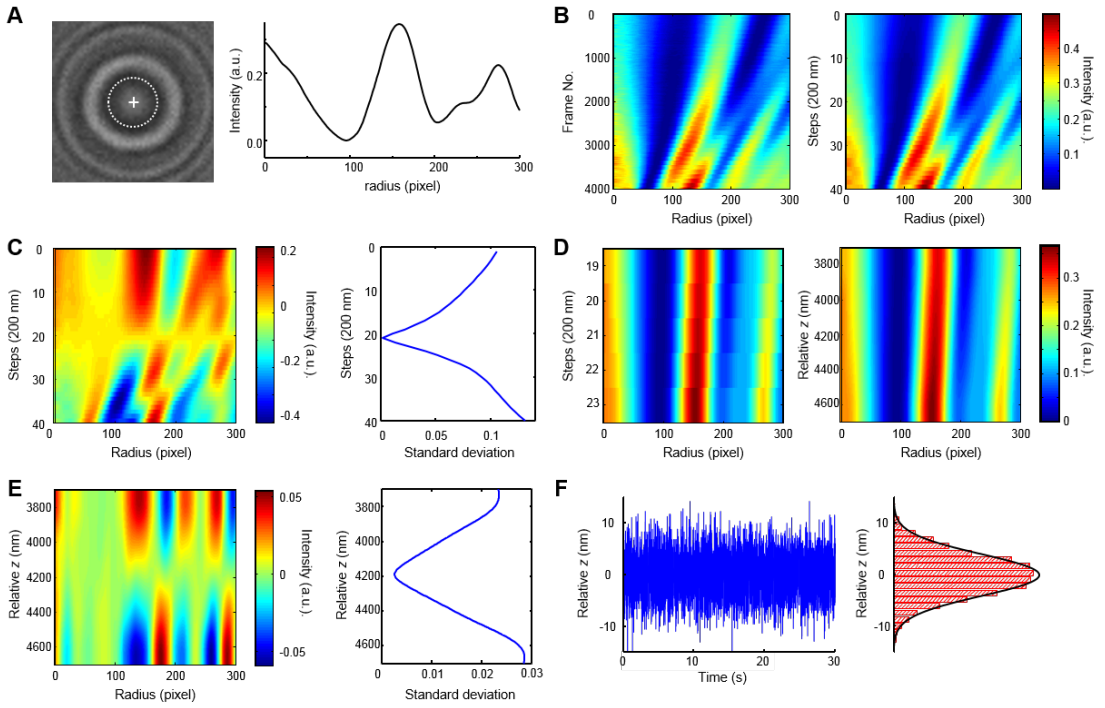

Fig. S3. Determination of *z* center position of a particle. (A) 100x enlarged transmission image of the particle (left) and its radially averaged radial intensity profile (right). The white cross on the transmission image is the fitted *xy* center position as in **Fig. S2**. **(B)** Measurement of a *z* calibration map. Each row on the left map is a radial intensity profile. The radial intensity profiles at the same *z* position (i.e., 100 frames) are averaged to form an averaged radial intensity profile. The averaged radial intensity profiles at all *z* positions are stacked to form the *z* calibration map on the right. **(C)** The

z calibration map after subtracting the radial intensity profile in the right panel of A from each row (left), and the standard deviation of each row after subtraction (right). For the specific example here, the 21st row gives the smallest standard deviation. **(D)** Left: the -2 to +2 rows of 21st step on the *z* calibration map in **C** (left). Right: the interpolation of the left color map by 200 times. **(E)** The interpolated *z* calibration curve after subtracting the radial intensity profile in **A** from each row (left), and the standard deviation of each row after subtraction (right). The relative *z* position (i.e., a single row) that gives the smallest standard deviation is the *z* position of the particle. **(F)** Left: fluctuation of the relative *z* position of a position marker after drift correction. Right: corresponding histogram of the relative *z* position and the Gaussian fitting (black curve), whose FMHM is ~13.4± 0.4 nm.

5.1.5. Magnetic Force Calibration: 10% error, and the expected force changes from particle movement during real-time polymer growth is ~0.5%

The magnetic force (F) is calibrated using polynorbornene tethered magnetic particles based on the fluctuation-dissipation theorem (*43*):

$$F = \frac{k_B T}{\langle \Delta x^2 \rangle} \Delta z \qquad \textbf{Eqn. S3}$$

Here k_B is the Boltzmann constant, T is temperature, Δz is the extension of the polymer tether, and $\langle \Delta x^2 \rangle$ is the variance of the tethered magnetic particle center position along the direction of external magnetic field that is transversal to the pulling force (x direction as indicated in **Fig. S1**).

Δz is measured by the z position of the magnetic particle relative to the z position where the particle is on the glass surface (**Fig. S4A**) (*38*). $\langle \Delta x^2 \rangle$ is calculated by averaging the Δx^2 values relative to the mean x position (**Fig. S4B**). Alternatively, $\langle \Delta x^2 \rangle$ can also be calculated through the power spectral density of the motion, which is obtained by Fourier-transformation of the x-vs.-t trajectory (**Fig. S4C**). Then the power spectral density is fitted by the following equation (*40, 44*):

$$S(f) = \frac{D}{\pi^2 (f^2 + f_c^2)} \qquad \textbf{Eqn. S4}$$

Here the power spectral density *S(f)* is a function of frequency f, D is the diffusion constant and f_c is the corner frequency. $\langle \Delta x^2 \rangle$ is then calculated by integrating the area under the fitted curve. The $\langle \Delta x^2 \rangle$ values obtained from both methods are in good agreement with each other (**Fig. S4D**), and we use the value determined from the direct averaging of experimental Δx^2 method for all following analysis.

As the configuration of the magnet set is fixed, the magnetic force is determined by the distance between magnet set and tethered particles along the z direction (*45*). In changing the magnetic force, the magnet set is moved by the z micro-stage with 50 μm step size, and the zero z magnet distance is where the magnets touch the upper surface of the flow cell (**Fig. S4E**) (the thickness of the flow cell does not vary much, about ±20 μm).

At each z magnet distance, 10,000 frames are recorded at 1ms exposure time and 200 Hz sampling frequency, and the magnetic force is calculated based on **Eqn. S3**. The magnetic force is then plotted against the z magnet distance and fitted by a single-exponential curve (**Fig. S4F**). The magnetic force has ~10% error due to errors

in z magnet distance and the size distribution of the magnetic particles.

It is important note that during our polymerization measurements, the extension of the growing polymer is less than a few μm in z, within which the magnetic force is essentially constant as long as the magnet positions are held. The magnetic force F is fitted as a function of z magnet distance:

$$F = Aexp(-\frac{z_m}{b}) \quad \textbf{Eqn. S5}$$

Here A is the scaling factor, b is the exponential decay constant and z_m is z magnet distance. Thus, the relative change of F within a small z magnet distance can be estimated by:

$$\frac{dF}{F} = -\frac{1}{b}dz_m \quad \textbf{Eqn. S6}$$

Based on the exponential fitting in **Fig. S4F**, b is 385.95 μm^{-1}. Assuming the polymer grew for 2 μm (dz_m = 2 μm), the relative change of F is ~ 0.5 %, which is much smaller than the error of magnetic force determination (~10%).

In measuring the magnetic force, 1 ms exposure time is used to minimize the smearing effect due to the thermally driven particle motions, which would result in an underestimation of $\langle \Delta x^2 \rangle$ (*45*). As shown in **Fig. S4G**, at ~4.5 pN magnetic force and 200 Hz sampling frequency, $\langle \Delta x^2 \rangle$ decreases dramatically when the exposure time becomes longer than 1 ms. However, the sampling frequency does not affect $\langle \Delta x^2 \rangle$ significantly (**Fig. S4H**) when the exposure time is fixed at 1 ms.

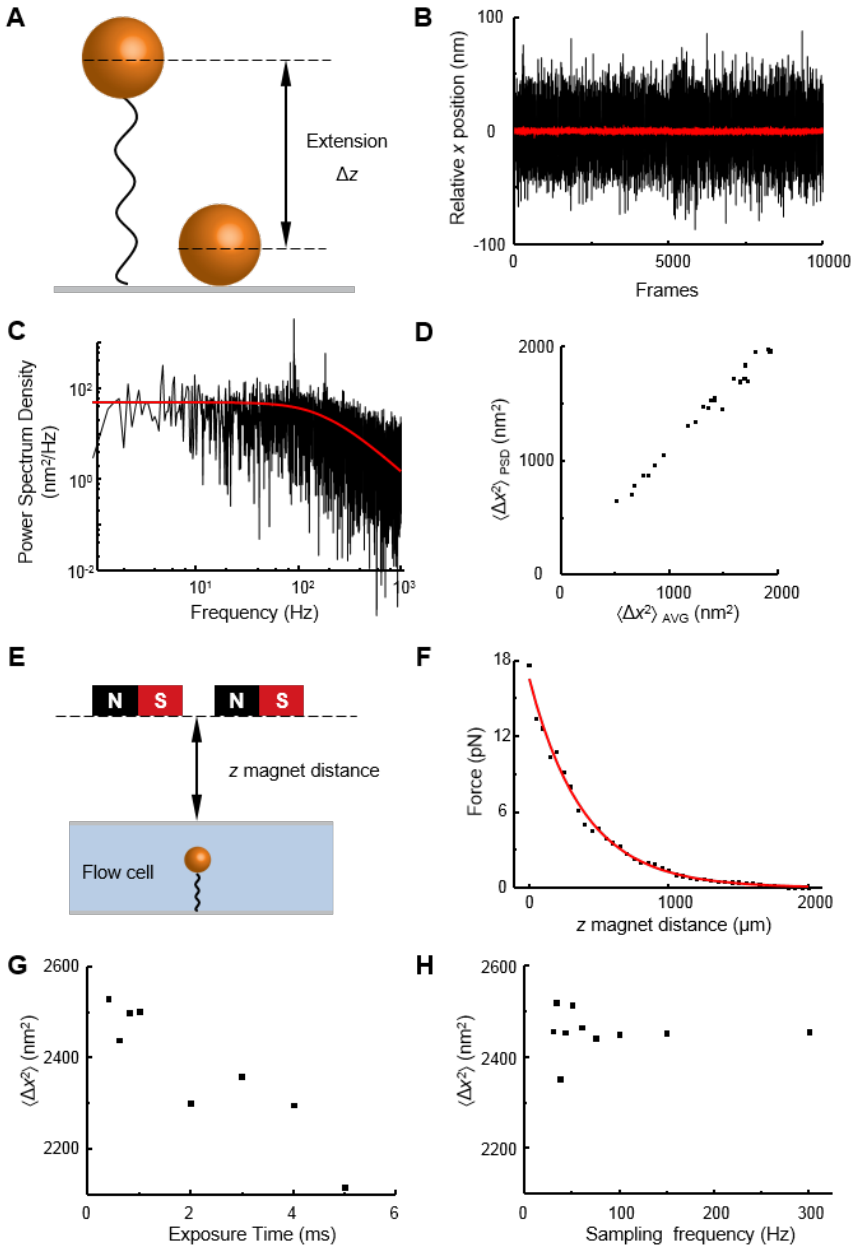

Fig. S4. (A) Illustration of extension measurement. **(B)** Black trajectory: fluctuation of the *x* position of a polynorbornene tethered particle, under the highest magnetic force (~16.7 pN); red trajectory: fluctuation of the *x* position of a position marker. **(C)** Fourier transformation of the black trajectory in **B**. **(D)** Comparison of $\langle \Delta x^2 \rangle$ values calculated by power spectral density method (PSD) and direct averaging (AVG). **(E)** Illustration of the definition of *z* magnet distance. **(F)** Magnetic force vs. *z* magnetic distance, in which

the force F is calculated based on **Eqn. S3** (black squares), and a single-exponential fitting (red curve). **(G)** Dependence of $\langle \Delta x^2 \rangle$ on the camera exposure time at the fixed 200 Hz sampling frequency. **(H)** Dependence of $\langle \Delta x^2 \rangle$ on the sampling frequency at the fixed 1 ms exposure time.

5.1.6. Instrument testing with DNA, worm-like chain model analysis, as well as conversion between extension, contour length and subunit numbers

5.1.6.1. Instrument testing with DNA

To test if the magnetic force and the extension Δz are determined reliably, we measured the force-extension curve of a ~5k bp DNA following the procedure by Neuman et al (*38*), and fitted it by the worm-like chain (WLC) model (*46, 47*) (**Fig. S5A**):

$$F = \frac{k_B T}{P}\left[\frac{1}{4}\left(1 - \frac{\Delta z}{L_0}\right)^{-2} - \frac{1}{4} + \frac{\Delta z}{L_0}\right] \qquad \textbf{Eqn. S7}$$

Here F is the magnetic force, k_B is the Boltzmann constant, T is temperature, p is the persistent length of DNA, Δz is the extension of DNA, L_0 is the contour length of DNA. The persistent length determined in our measurement is 54.5 ± 3.2 nm as expected (~50 nm) (*48*). The contour length is 1791 ± 3 nm, as expected for a 5256 bp DNA (~1787 nm, ~0.34 nm per base pair (*38*)). The results indicate that the magnetic force as well as the extension and z center position of the magnetic particle are determined correctly.

The linear 5256 bp DNA used in this measurement (with a final length of 5256 bp) was PCR-cloned out of the pETDue-1 plasmid (Novagen) using two primers

(Integrated DNA Technologies), Forward primer: 5'-Biotin-GGGAATTGTGAGCGGATAACAATTCCC-3'. Reverse primer: 5'-Digoxigenin-GCTTGTTTCGGCGTGGGTATG-3'. The primers included a biotin and digoxigenin tags for later linkage. The PCR was carried out using the AccuPrime Pfx DNA Polymerase Kit (Life Technologies) with the following condition: a denaturation step at 95°C for 2 minutes, followed by 30 cycles of 15 seconds at 95°C, 30 seconds at 55°C, and 6 min at 68°C using the AccuPrime Pfx DNA polymerase. The PCR product was purified using Wizard SV Gel and PCR Clean-Up System (Promega), and its length was confirmed by 1% agarose gel.

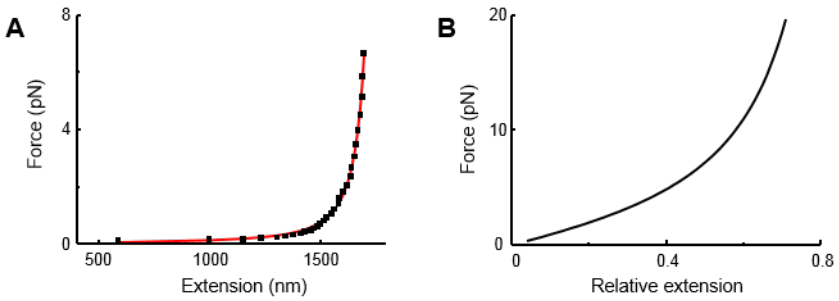

Fig. S5. (**A**) Force-extension measurement of a 5k bp DNA molecule (black square) and the WLC model fitting (red curve). The persistent length is determined to be 54.5 ± 3.2 nm, and the contour length is determined to be 1791 ± 3 nm. (**B**) The relationship between relative extension $\Delta z/L_0$ of polynorbornene and the magnetic force F.

5.1.6.2. Converting extension to contour length and number of monomers based on worm-like chain model

Eqn. S7 can be rearranged to give:

$$\left[\frac{1}{4}\left(1-\frac{\Delta z}{L_0}\right)^{-2}-\frac{1}{4}+\frac{\Delta z}{L_0}\right]=\frac{pF}{k_BT} \qquad \textbf{Eqn. S8}$$

Thus, the relative extension $\Delta z/L_0$ is only a function of magnetic force *F* and *T* and remains constant under constant force and temperature for a polymer with persistence length *p*. To convert the extension Δz to contour length L_0, we only need to know the value of persistent length *p*, the magnetic force *F*, and the temperature *T*. The magnetic force *F* is externally calibrated as mentioned above, and the temperature is room temperature (295 K). The persistent length *p* is determined by the WLC fitting of a polymer's force-extension curve after the polymerization reaction is stopped. With known persistent lengths (~0.71 nm for polynorbornene in **Fig. 1D**, and ~0.88 nm for polycyclooctene **Fig. S34M**), the relative extension $\Delta z\ /L_0$ under different forces can be calculated by solving **Eqn. S8**. An exemplary plot of F vs. $\Delta z\ /L_0$ is shown in **Fig. S5B**, using the persistent length of polynorbornene (0.71 nm).

Contour length can be further converted into the number of subunits provided the length of a subunit, which can be calculated based on the theoretical bond lengths and bond angles. The length of a polynorbornene subunit is ~0.62 nm (*49*), and the length of a polycyclooctene subunit is ~0.90 nm (*50*).

5.2. Sample preparation

5.2.1. Silica-coating of polystyrene magnetic particles

To minimized the interactions between the magnetic particle and the polynorbornene (or polycyclooctene) chain, the magnetic particles, which are made of polystyrene with iron oxide cores (Dynabeads® MyOne™ SILANE, Thermo Fisher

Scientific, 37002D), are coated with a silica shell following the Stöber process (*51*) (**Fig. S6**). The detailed procedure is as follows:

(1) Disperse 300 μL stock solution of magnetic particles in 25 mL water-ethanol mixture solvent (ethanol:water = 4:1 volume ratio).

(2) Add 400 μL TEOS (tetraethyl orthosilicate; Sigma Aldrich, 131903) and 100 μL 1 M NaOH solution to the mixture.

(3) Sonicate the solution for 3 hours, and then rinse the magnetic particles using deionized water for 5 times.

(4) Re-disperse the magnetic particles in 25 mL water-ethanol mixture solvent (ethanol:water = 4:1 volume ratio), and add 100 μL TEOS and 100 μL 1 M NaOH solution.

(5) Sonicate the solution for 1 hour, and rinse the magnetic particles using deionized water for 5 times. The resulting final particles have approximately 200 nm silica coating judging from their size increases by SEM (**Fig. S6B** vs. **A**).

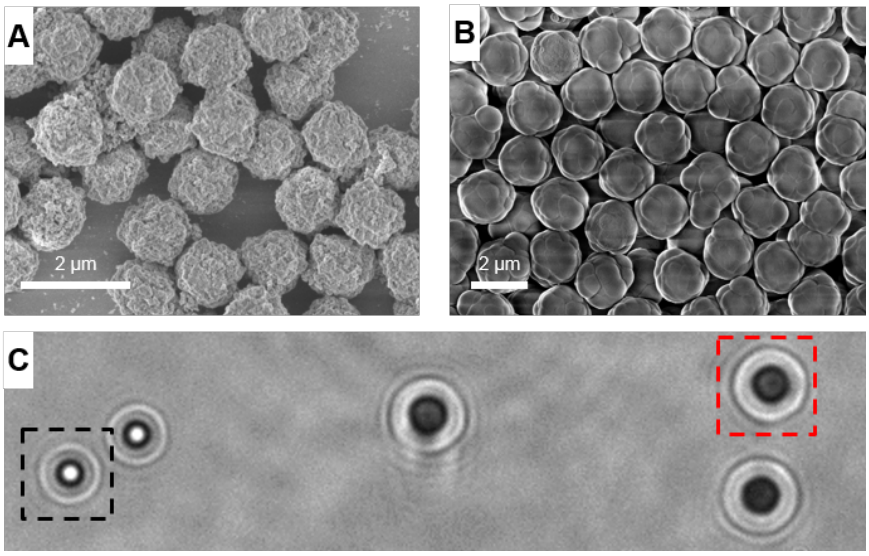

Fig. S6. (**A**) SEM image of the as-purchased polystyrene magnetic particles. (**B**) SEM image of silica-coated magnetic particles. (**C**) Bright field transmission image of polystyrene magnetic particles (e.g., the one in black dashed-line box) and silica-coated magnetic particles (e.g., the one in red dashed-line box) in toluene. They look distinctively different. The silica-coated ones are darker and larger. Polystyrene magnetic particles are used as position markers, and silica-coated magnetic particles are loaded with G2 catalyst.

5.2.2. Synthesis of Grubbs' 2nd generation catalyst whose NHC ligand is modified with silane groups

5.2.2.1. Synthetic route

Scheme S1 outlines the synthetic procedures for modifying the NHC ligand of the G2 catalyst with alkyloxysilane groups (compound **7**) to be immobilized on the silica surface of the magnetic particle (or a glass coverslip). Compounds **3-6** were previously reported in the literature; compound **7** was also reported in previous

literature but not characterized (see below).

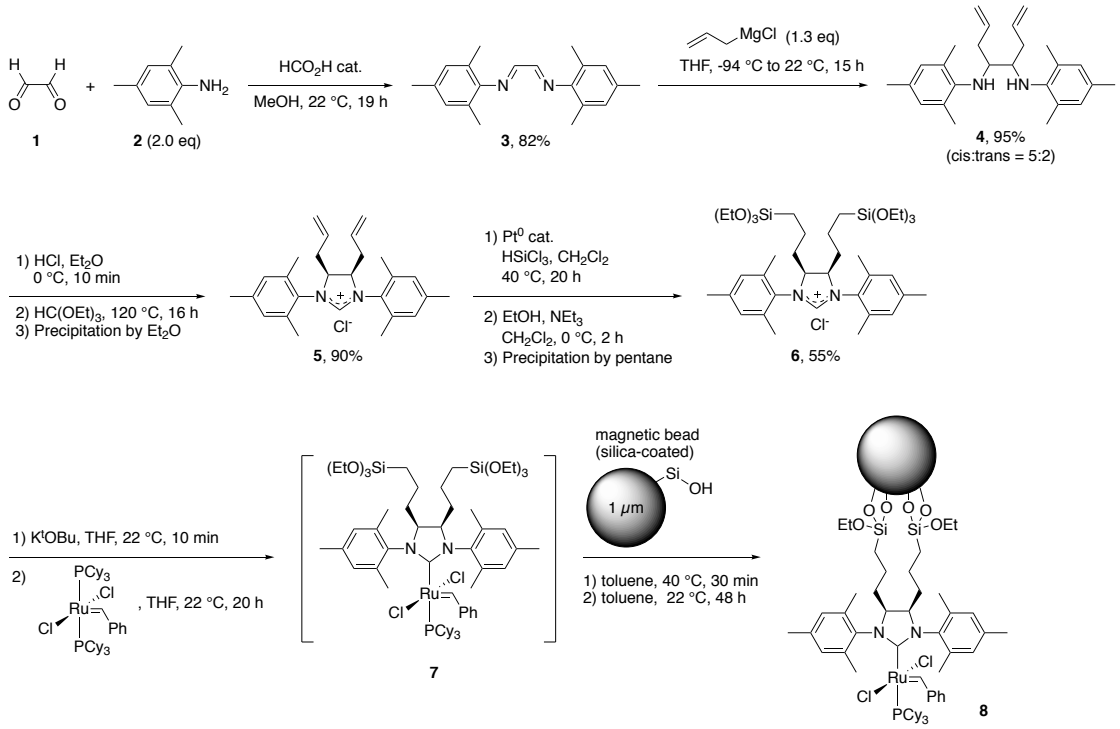

Scheme S1. Synthetic scheme of modifying the NHC ligand of the Grubbs II catalyst

5.2.2.2. Materials and general information

Toluene, THF, and dichloromethane were dried by passage through solvent purification columns containing activated alumina, and degassed before use. Triethylamine and ethanol were dried over molecular sieves. Formic acid was purchased from Mallinckrodt chemicals (#2592-05) and used as received. Other chemicals were purchased from Aldrich and used as received: glyoxal solution 40wt% in water (compound **1**), #128465; 2,4,6-trimethylaniline (compound **2**), #132179; allylmagnesium chloride solution 2.0 M in THF, #225908; hydrogen chloride solution 2.0 M in ether, #455180; triethyl orthoformate anhydrous 98%, #304050; platinum (0)-1,3-divinyl-1,1,3,3-tetramethyldisiloxane complex solution in xylene Pt~2%,

#479519; trichlorosilane, #175552; Grubbs catalyst 1st generation, #579726; Grubbs catalyst 2nd generation, #569747.

All manipulations of air and water sensitive compounds were carried out under nitrogen in a Braun Labmaster glovebox or by using standard Schlenk line technique. ^{1}H and ^{13}C NMR spectra were recorded on MERCURY 300 (^{1}H, 300 MHz, ^{13}C, 75 MHz) or INOVA 600 (^{1}H, 300 MHz). Chemical shifts are reported in parts per million (ppm) downfield from tetramethylsilane (TMS) with reference to internal solvent for ^{1}H NMR and ^{13}C NMR spectra. Multiplicities are abbreviated as follows: singlet (s), doublet (d), triplet (t), quartet (q), quintet (quint), septet (sept), multiplet (m), and broad (br).

5.2.2.3. Synthesis of 3 (*52*)

To a solution of **2** (2.7 g, 2.8 mL, 20 mmol) in methanol (10 mL), **1** (0.58 g, 10 mmol) was added. Ten drops of HCO_2H was then added, and stirred at room temperature for 19 hours. The solution was then filtered and the remaining solid was washed with methanol to obtain **3** (2.4 g, 82%) as a bright yellow powder. Proton and carbon NMR spectra matched those previously reported in reference (*52*).

^{1}H NMR ($CDCl_3$, 300 MHz; **Fig. S7**, upper): δ = 2.16 (s, 12H), 2.29 (s, 6H), 6.91 (s, 4H), 8.10 (s, 2H).

^{13}C NMR (75 MHz, $CDCl_3$; **Fig. S7**, lower): δ = 18.4, 20.9, 126.7, 129.1, 134.4, 147.6, 163.6.

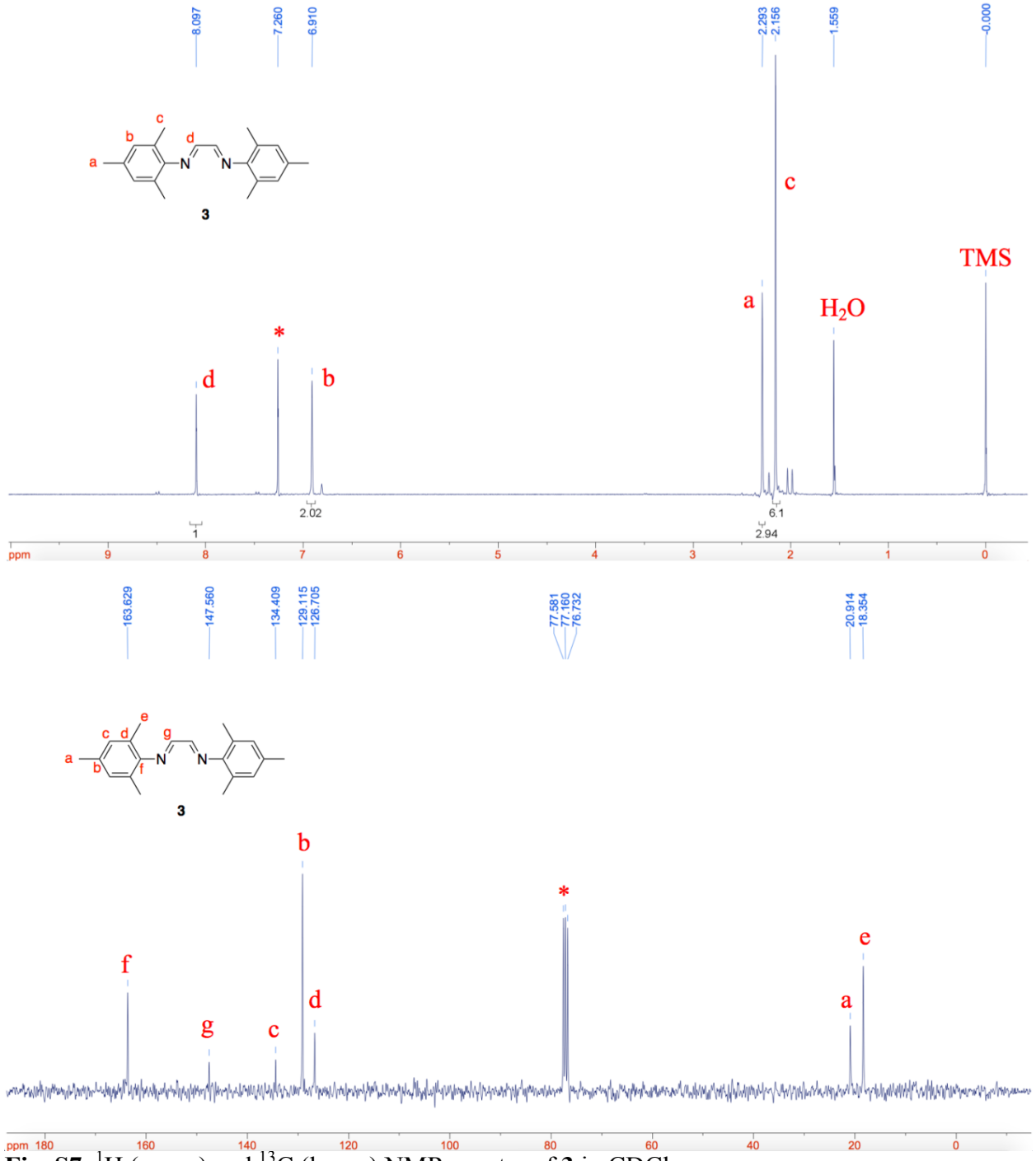

Fig. S7. ^{1}H (upper) and ^{13}C (lower) NMR spectra of **3** in $CDCl_3$.

5.2.2.4. Synthesis of 4 (*53*)

In a flame dried 300 mL round-bottom flask under N_2 atmosphere, bisimine **3** (2 g, 6.83 mmol) was added and dissolved in 100 mL of dry THF. The solution was cooled to −78 °C using a dry ice/acetone bath and then allyl magnesiumchloride (2 M in THF, 8.6 mL, 17.2 mmol) was added dropwise via a syringe. After the addition, the cold bath was removed and the mixture was stirred overnight while warming to room temperature. Then the reaction was quenched by the addition of saturated aq. NH_4Cl solution. The mixture was evaporated to remove THF, then diluted with Et_2O (50 mL), and the organic layer was separated. The aqueous layer was extracted with Et_2O (50 mL × 3) and the combined organic extracts were washed with water, brine and dried over Na_2SO_4 and then concentrated to give compound **4** (2.70 g, quant) as a yellow oil. Note that **4** has two chiral carbons, and it is a mixture of diastereomers (cis: trans = 5:2). The ratio of cis and trans stereoisomers was calculated by comparing the integration value of ^{1}H NMR peak at 6.8 ppm. Proton and carbon NMR spectra matched those previously reported in reference (*53*).

^{1}H NMR (300 MHz, $CDCl_3$; **Fig. S8**, upper): δ = 2.22 (s, 6H), 2.23 (s, 12H), 3.70 (s, 2H), 5.00-5.10 (m, 4H), 5.76 (m, 2H), 6.79 (s, 4H).

^{13}C NMR (75 MHz, $CDCl_3$; **Fig. S8**, lower): δ = 19.2, 19.6, 20.6, 35.9, 36.2, 57.8, 58.4, 116.9, 128.6, 129.9, 130.3, 136.2, 136.4, 141.5, 141.9.

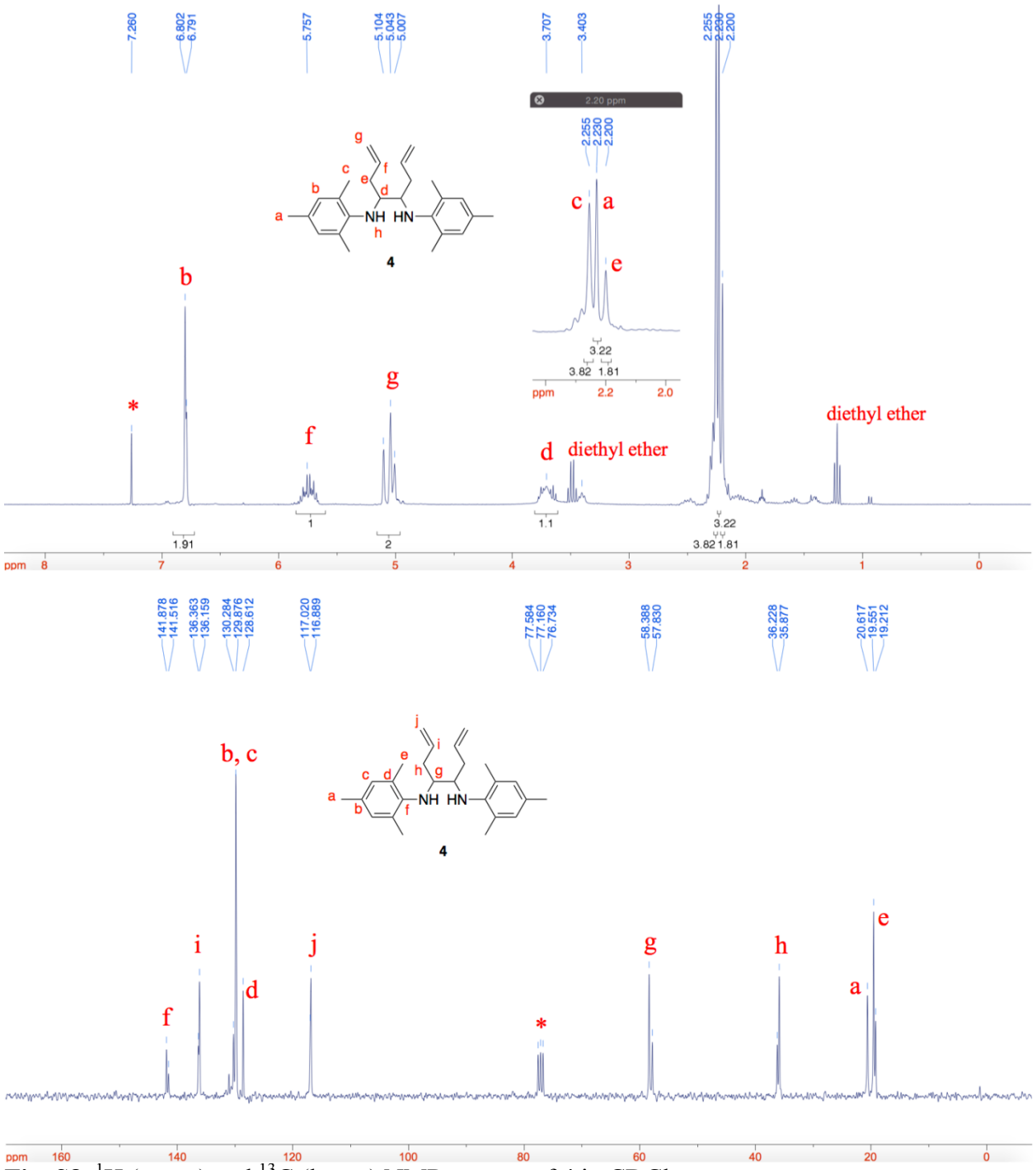

Fig. S8. ^{1}H (upper) and ^{13}C (lower) NMR spectra of **4** in $CDCl_3$.

5.2.2.5. Synthesis of 5 (*54*)

In a 100 mL flame dried round-bottom flask under N_2 atmosphere, diamine **4** (2.58 g, 6.85 mmol) was dissolved in 25 mL of Et_2O and cooled to 0 °C. This solution was treated with a solution of HCl (2 M in Et_2O, 4 mL, 8 mmol) to precipitate the diamine hydrochloride salt. The solid was isolated by filtration and washed with Et_2O several times and then placed back into the round-bottom flask and quickly dried. To this solid, triethylorthoformate (15.0 mL, 102 mmol) was added via a syringe, and the mixture was heated at 120 °C for 16 hours. Then the mixture was cooled, and most volatiles were removed under vacuum on Schlenk line. The product was precipitated by Et_2O, filtered, washed with Et_2O and EtOAc and finally pentane, and then dried under vacuum to obtain compound **5** (2.92 g, 95%) as an off-white solid. The product had pure cis stereoisomer, probably due to precipitation from ether. Proton and carbon NMR spectra matched those previously reported in reference (*54*).

^{1}H NMR (300 MHz, $CDCl_3$; **Fig. S9**, upper): δ = 2.28 (s, 6H), 2.39 (s, 6H), 2.49 (m, 10H), 4.92-5.08 (m, 4H), 5.44-5.50 (m, 2H), 6.93 (s, 2H), 6.96 (s, 2H), 10.60 (s, 1H).

^{13}C NMR (75 MHz, $CDCl_3$; **Fig. S9**, lower): δ = 18.8, 19.3, 21.2, 31.5, 65.6, 119.0, 129.4, 130.3, 130.5, 132.0, 134.9, 135.6, 140.4, 160.4.

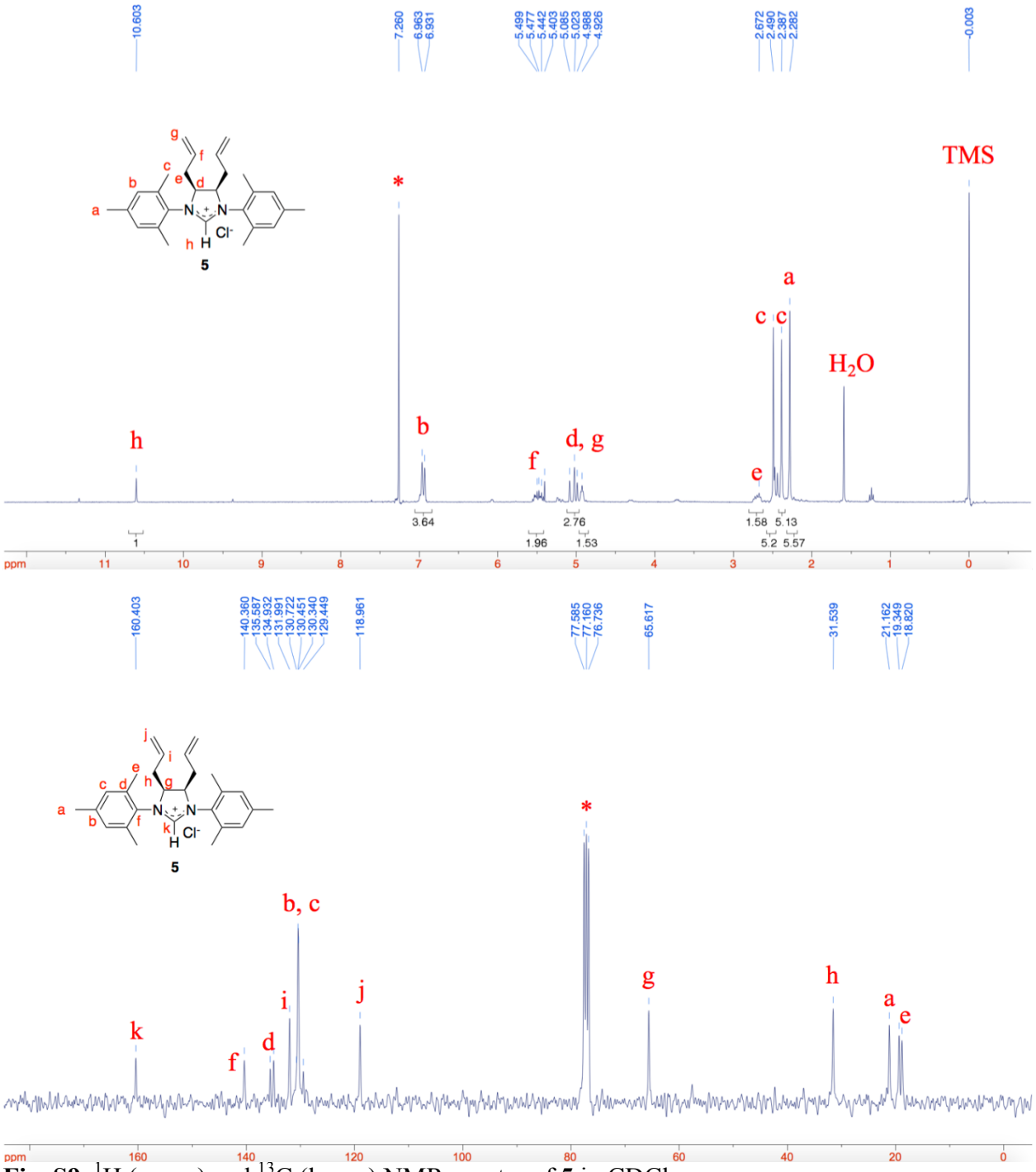

Fig. S9. ^{1}H (upper) and ^{13}C (lower) NMR spectra of **5** in $CDCl_3$.

5.2.2.6. Synthesis of 6 (*54*)

In a 100 mL round bottom flask, compound **5** (500 mg, 1.18 mmol) was dissolved in dry CH_2Cl_2 (10 mL) under N_2 atmosphere. To this solution Karstedt's catalyst (2% Pt in xylene, 700 μL, 0.070 mmol) and $HSiCl_3$ (3.50 mL, 34.7 mmol) were added, and the reaction was stirred under N_2 at 40°C for 20 h. The excess $HSiCl_3$ was distilled off, and the residue was redissolved in CH_2Cl_2 and the mixture was cooled to 0 °C. Then a mixture of anhydrous EtOH/NEt_3 (1/1, v/v, 9 mL) was added and the solution was stirred at room temperature for 2 h. The volatiles were then removed under vacuum, and the residue was treated with dry toluene and filtered to separate the ammonium salt. Filtrates were concentrated under vacuum and dry pentane was added to precipitate the desired product, which was separated by filtration and further washed several times with pentane to obtain compound **6** as a cream-colored powder (497 mg, 56%). Proton and carbon NMR spectra matched those previously reported in reference (*54*).

^{1}H NMR (300 MHz, $CDCl_3$; **Fig. S10**, upper): δ = 0.52 (m, 4H), 1.15 (t, 18H, *J* = 6.9Hz), 1.28 (m, 4H), 1.75 (br s, 2H), 1.85 (br s, 2H), 2.26 (s, 6H), 2.36 (s, 6H), 2.47 (s, 6H), 3.70 (q, 12H, *J* = 6.9Hz), 4.62 (s, 2H), 6.92 (s, 2H), 6.96 (s, 2H), 10.6 (s, 1H).

^{13}C NMR (75 MHz, $CDCl_3$; **Fig. S10**, lower): δ = 10.7, 18.4, 18.7, 19.2, 20.7, 21.2, 30.2, 58.5, 66.1, 130.0, 130.4, 130.5, 134.6, 135.8, 140.0, 160.7.

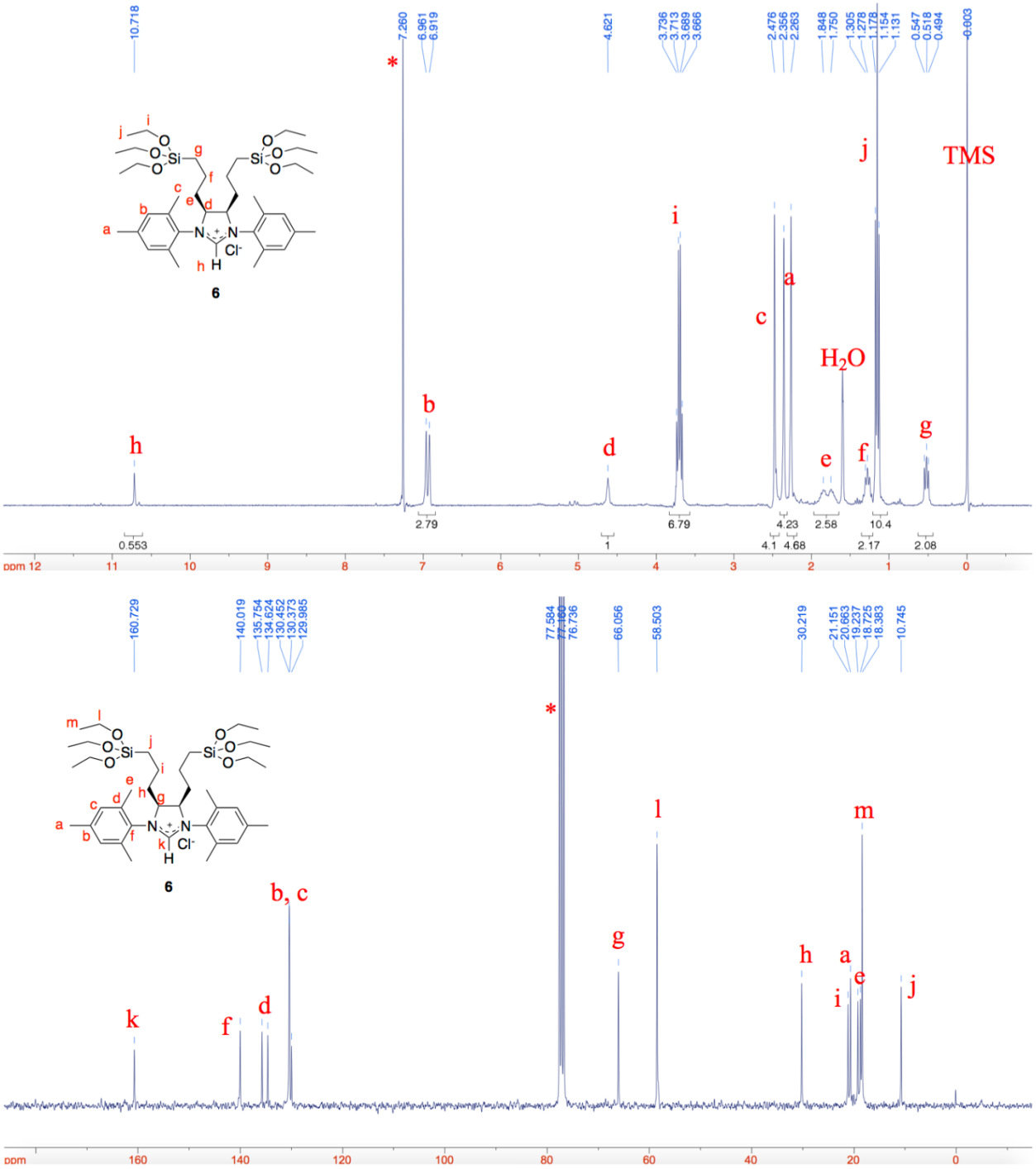

Fig. S10. ^{1}H (upper) and ^{13}C (lower) NMR spectra of **6** in $CDCl_3$.

5.2.2.7. Synthesis of 7 (*55*)

The ligand exchange reaction to obtain the modified G2 catalyst **7** from the 1st generation Grubbs' catalyst following literature (*55*). In a 20 mL glass vial under N_2 atmosphere, compound **6** (10 mg, 0.013 mmol) was dissolved in dry and degassed THF. To the solution dry KO^{t}Bu (1.5 mg, 0.013 mmol) was added, and stirred at room temperature for 10 min. After the color of the solution changed to yellow, the 1st generation Grubbs' catalyst (G1 catalyst; 10 mg, 0.011 mmol) was added, and the mixture was stirred in a glove box at room temperature for 20 h. Then the vial was removed from the glove box, and dried under vacuum to obtain a mixture of compound **7** and G1 catalyst. Formation of **7** was confirmed by ^{1}H NMR of the reaction mixture (Section 5.2.2.8). As the compound **7** was difficult to purify and the yield was low, the mixture was used directly for the next reaction without further purification. The remaining G1 catalyst in the mixture will be removed through washing after immobilizing the modified G2 catalyst on the magnetic particle (see below).

It is worth noting that a previous study (*56*) also synthesized compound **7** by first immobilizing compound **6** on the particles before performing the ligand exchange. The resulting compound **7** there was on the particle directly and could not be characterized. Our approach of performing ligand exchange before immobilization allowed us to check the formation of the compound **7** via NMR (see Section 5.2.2.8 below).

5.2.2.8. Characterization of 7 and variable temperature ^{1}H NMR experiment.

We used ^{1}H NMR to confirm the formation of **7**, the G2 catalyst with a modified NHC ligand synthesized via a ligand change reaction with the G1 catalyst (**Scheme S1**). As seen **Fig. S11**, the reaction mixture of compound **7** and Grubbs 1st generation catalyst has three peaks from Ru=C*H*Ph at –20 °C. The peak at around 20 ppm comes from Grubbs 1st generation catalyst, and other two peaks around 19 ppm are attributed to **7**. The two peaks likely reflect different conformers that result from rotational hindrance caused by the bulky modified NHC ligand, as seen in previous literature (*57*). To confirm that the two peak pattern of the Ru=C*H*Ph of compound **7** indeed results from different conformers, we measured the ^{1}H NMR from –20 °C to 60 °C (**Fig. S11**). With increasing temperature, the two peaks first broaden and eventually merged into one peak at 60 °C, supporting that the two-peak pattern results from the rotational hindrance of bulky NHC ligand.

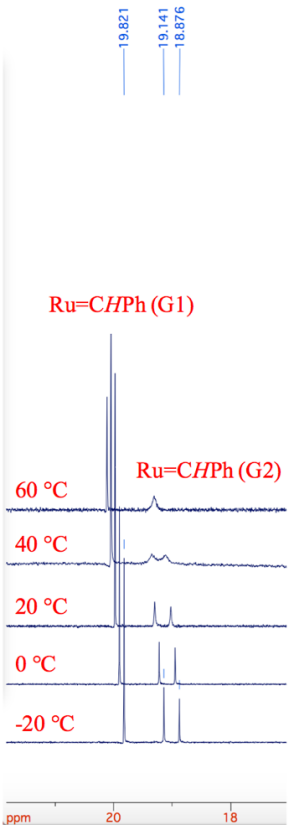

Fig. S11. Variable temperature ^{1}H NMR spectra of **7** in $CDCl_3$.

5.2.3. Immobilization of modified G2 catalyst on silica-coated magnetic particles

5.2.3.1. Preparation of 8

In a 10 mL round bottom flask under N_2 atmosphere, the suspension of silica-coated magnetic particles and the solution of compound **7** (each of them in 1 mL of toluene) were added via cannula transfer. Then the mixture was stirred at 35 °C for 2 days. A magnet was used to precipitate the magnetic particles to remove the supernatant, and the particles were washed 10 times with dry toluene to remove unattached modified G2 catalyst as well as the G1 catalyst from the synthesis of **7**. The particles were separated into 10 vials, dried under vacuum overnight. The structure of compound **8** in the scheme is for schematic illustration only.

5.2.3.2. Romp activity test of 8

We checked whether the catalyst **8** immobilized on the magnetic particle is active for ROMP. To the suspension of catalyst **8** in toluene (5 mL), 1 M solution of norbornene (1 mL) was injected, and the reaction solution was stirred at room temperature. After 30 minutes of stirring, ethanol was added to precipitate the polymer. The polymer was dried, re-dissolved in toluene, and then ethyl vinyl ether was added in order to cleave the catalyst from the polymer. The catalyst-loaded particle was collected using a magnet, and the supernatant was taken out, then dried under vacuum. The residue was characterized by ^{1}H NMR to confirm the formation of polynorbornene (**Fig. S12**, middle).

As a control, after the preparation of **8**, the last toluene washing solution (1 mL) was taken out, and 1 M solution of norbornene in toluene (0.1 mL) was injected. The mixture was stirred for 1 h, then dried by nitrogen blow. ^{1}H NMR of the residue shows no signal from polynorbornene (**Fig. S12**, bottom). This control experiment indicates that the leftover G1 catalyst in the ligand exchange reaction was not immobilized onto the magnetic particle and was completely washed out, making no contribution to the subsequent ROMP activity.

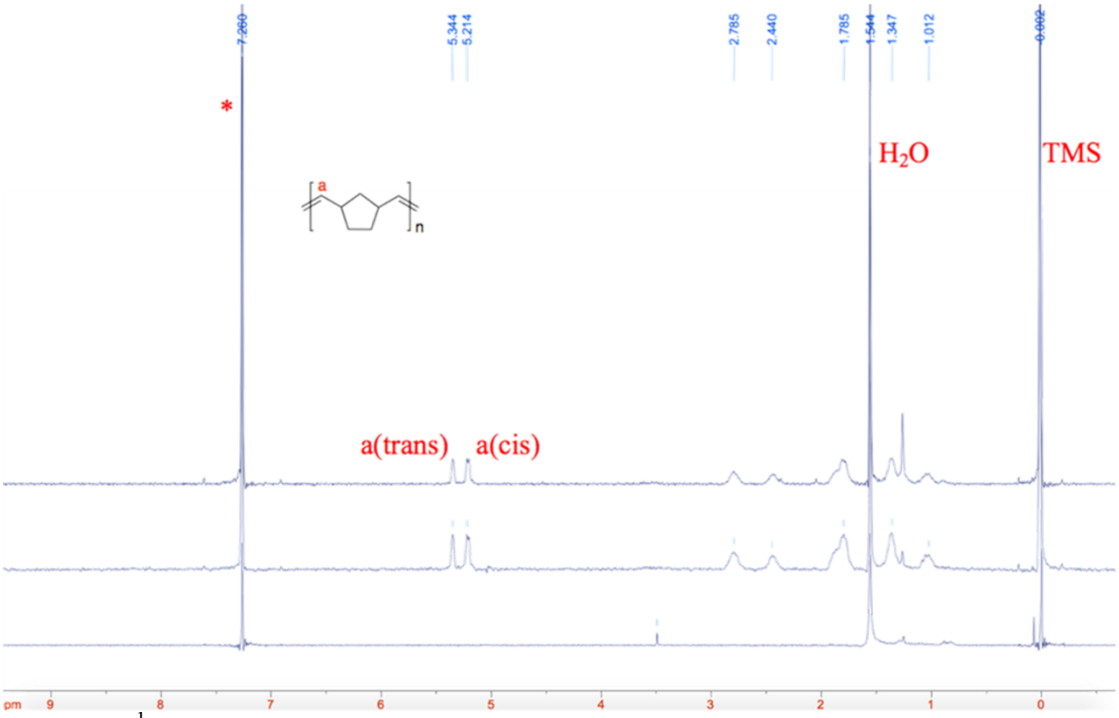

Fig. S12. ^{1}H NMR spectrum in $CDCl_3$ of ensemble polymerization reaction product using catalyst **8** and norbornene to form polynorbornene (middle), in comparison with that of polynorbornene formed from ROMP of norbornene catalyzed by the commercial Grubbs 2nd catalyst (top). Also, no polynorbornene was detectable in the reaction mixture of norbornene and washing solution of the catalyst **8** (bottom).

5.2.4. Preparation of norbornene and polynorbornene functionalized glass coverslip

5.2.4.1. Glass coverslip cleaning

Place glass coverslip (VWR, No. 1, 24 mm × 60 mm, 48393-106) in a Teflon staining jar that holds the coverslip vertically. Sonicate the coverslip in detergent solution (Alconox, 1104) for 30 min at ~60°C. Pour out the detergent solution, and flush the coverslips vigorously using tap water to remove residual detergent. Rinse the

coverslips with deionized water (18.2 MΩ/cm), and dry with N_2.

5.2.4.2. Position marker immobilization

Position markers (Dynabeads® MyOne™ SILANE, Thermo Fisher Scientific, 37002D) immobilized on the glass coverslip are used to corrected for the drift caused by the movement of sample stage or microscope objective. The procedure to fix the position markers on glass coverslip is as follows:

(1) Dilute the stock solution of position marker by 1000 times in water.

(2) Add the diluted solution of position marker dropwise on the cleaned glass coverslip and incubated for 30 minutes.

(3) Dry the glass coverslip with N_2, and bake at 200℃ for at least 2 hours.

5.2.4.3. Surface functionalization of glass coverslip

The surface of the glass coverslip is first functionalized with norbornene-silane reagent ([(5-bicyclo[2.2.1]hept-2-enyl)ethyl]trimethoxysilane; Gelest, SIB0988.0) using vapor reaction. G2-loaded magnetic particles can directly react with immobilized norbornene through metathesis and get tethered to the glass coverslip, from which we observed single-polymer growth. However, the tethering efficiency was very low, likely because the tethering reaction happens between two solid surfaces.

To improve tethering efficiency, we further made from the norbornene-functionalized coverslip short polynorbornene (or polycyclooctene when *cis*-cyclooctene was used as monomer for single polymer visualization) chains, which facilitates the tethering of the catalyst-loaded magnetic particles to the coverslip surface

by providing more C=C reactive sites and more flexibility (**Scheme S2**). The detailed procedure is as follows:

(1) Place glass coverslips with position markers in a Teflon staining jar.

(2) Add 200 μL norbornene-silane into the Teflon cover glass holder.

(3) Put the Teflon staining jar, without cap, into a glass vacuum chamber (custom made), vacuum for ~2 hours at ~80 mTorr, then fill the chamber with N_2. There is still remaining silane solution in the jar over the vacuum process.

(4) Leave the vacuum chamber in an oven for ~1 hour at 90 ℃.

(5) Take the coverslips out and rinse with acetone and deionized water, and dry with N_2.

(6) Immerse the coverslips into a toluene solution of G2 catalyst (Sigma Aldrich, 569747), and react for ~15 minutes. Rinse with toluene to remove the non-reacted G2 catalysts.

(7) Immerse the coverslips into a toluene solution of norbornene (~0.5 M) (Sigma Aldrich, N32407) or *cis*-cyclooctene (~0.5 M) (Sigma Aldrich, 125482), and react for ~15 minutes to grow short polynorbornene chains. For experiments of polycyclooctene, a toluene solution of cyclooctene (~0.5 M) is used instead. Then cleave off the G2 catalyst using ethyl vinyl ether (Sigma Aldrich, 422177). Rinse with toluene and dry with N_2.

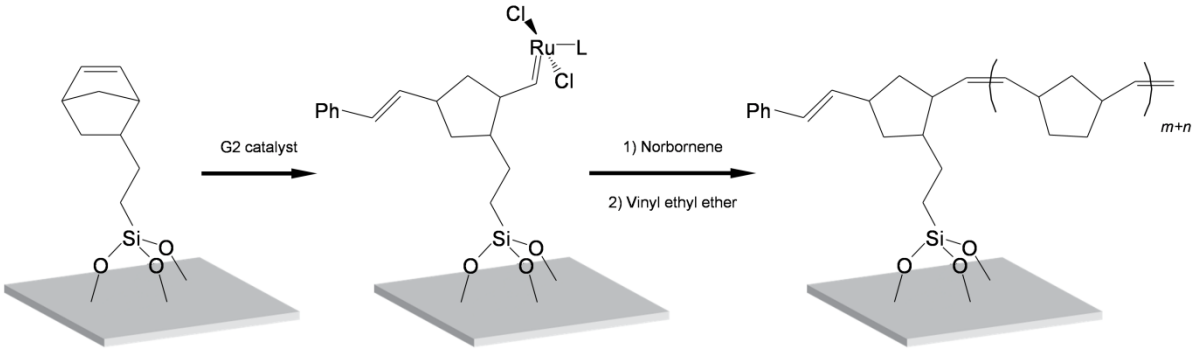

Scheme S2. Functionalization of glass coverslip by polynorbornene. G2 catalyst: Grubbs' 2nd generation catalyst; L: *N*-heterocyclic carbine ligand.

5.3. Single-polymer growth experiment

5.3.1. Reaction flow cell assembly

The single-molecule polymer growth experiments are done in a nitrogen protected flow cell device, as shown in **Fig. S13**.

The bottom of the flow cell is a polynorbornene-functionalized glass coverslip (24×60 mm) with position markers. The top is a glass coverslip that is cut to a smaller size (12×48 mm). The top glass coverslip is attached to the bottom coverslip by double-sided tap on the four corners of the top coverslip to form the sample chamber. A small piece of glass slide (home-cut ~0.4×0.4 inch, VWR Micro Slides, 48300-037) is used to connect ethylene oxide micro-tube (Scientific Commodities Inc., BB31695-PE/4) to the flow cell. The micro-tube is inserted into the hole in the middle of the glass slide, and the glass slide is then attached to the top of the flow cell (the larger coverslip) using double-sided tap. After the glass pieces are taped together, junctions and opening area are sealed using epoxy super glue.

The inlet micro-tube is connected to an air-tight glass vial (Chemglass, CV-5323-1232), and the outlet micro-tube is connected to a 5 mL air-tight glass syringe (Hamilton, Gastight #1005). Solutions are injected into the air-tight glass vial using air-tight glass syringes (Hamilton, Gastight #1001), and then flown into the sample chamber by sucking the 5 mL air-tight glass syringe. The motion of the 5 mL air-tight glass syringe is controlled by a syringe pump (Chemyx, Fusion 200).

A nitrogen balloon is connected to the air-tight glass vial through a micro-tube. The nitrogen balloon not only keeps the whole flow cell in inert atmosphere, but also maintains constant pressure during sample injection and flow.

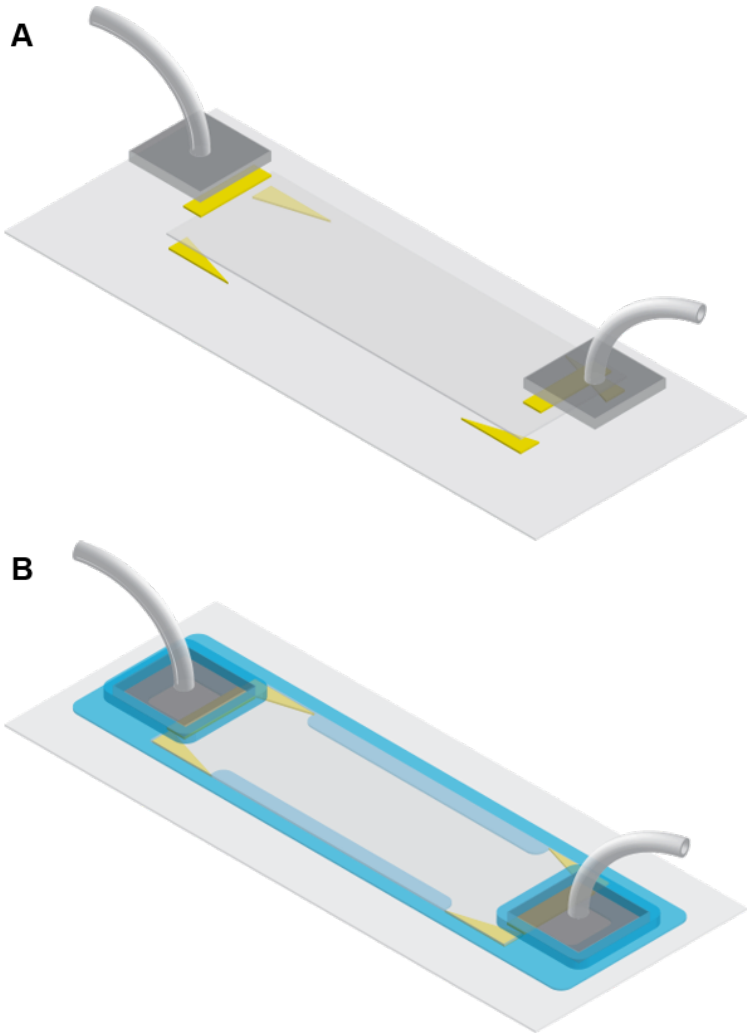

Fig. S13. Schematic diagram of the flow cell. (**A**) Components of the flow cell. Glass coverslips are in light grey. The larger coverslip on the bottom is functionalized with polynorbornene (or polycyclooctene) and deposited with position markers. Glass slides with holes are in dark grey. Double-sided tapes are in yellow. (**B**) Assembled flow cell. Epoxy super glue area is in blue.

5.3.2. Tethering of G2-loaded magnetic particles to functionalized glass coverslip surface

To tether the G2-loaded magnetic particles to the glass coverslip, ~200 μL toluene solution of G2-loaded magnetic particles was flown into the flow cell at 100 μL/min, and incubated for ~15 minutes. Then 1 mL toluene was used to wash away non-tethered particles at 100 μL/min under magnetic force (~5 pN).

The tethering reaction is through a metathesis reaction, illustrated in **Scheme S3**. G2 catalyst immobilized on the magnetic particle is activated after the PCy_3 ligand falls off spontaneously, and then reacts with one of the C=C bonds in a polynorbornene on the glass surface, which cleaves the polynorbornene chain. This metathesis reaction gives the magnetic particle a 50% chance to get tethered to the glass surface, and the other 50% chance to leave the surface with the cleaved polymer chain.

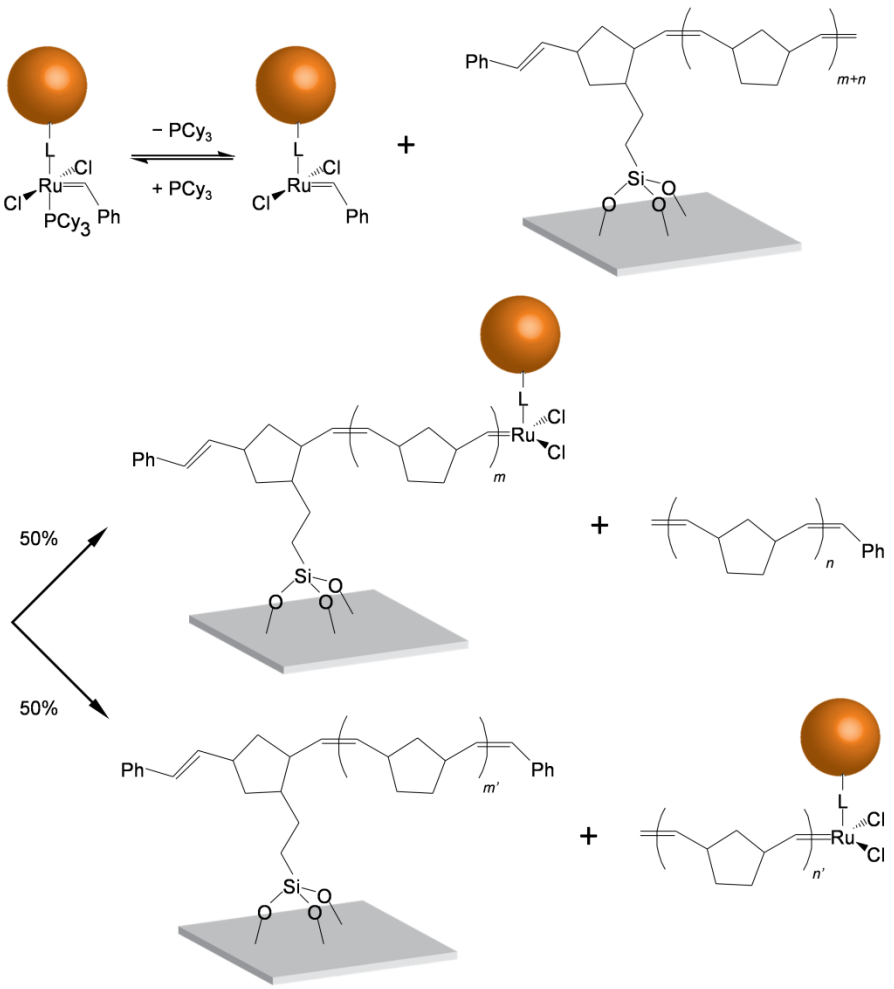

Scheme S3. Tethering of G2-loaded magnetic particles to polymers (e.g., polynorbornene) immobilized on glass surface via metathesis reaction. In the metathesis reaction, the magnetic particle has a 50% chance to become tethered to the glass. L: *N*-heterocyclic carbene ligand.

5.3.3. Real-time visualization of single polymer growth

Real-time growth traces were recorded at 2 Hz sampling frequency and 1 ms exposure time. Before monomer addition, the flow cell sample was placed under magnetic force for ~15 minutes to further remove the nonspecifically adsorbed particles and stretch out potential nonspecific interactions between the magnetic particles and the

coverslip surface. After the *z* position of polymer-tethered magnetic particles were stable for at least 10 minutes, 200 μL monomer solution was flown into the flow cell at 100 μL/minute rate to initiate the growth of the polymer tether.

Rotation of magnetic particles before and after polymer growth was done by rotating the magnets at 120 degrees per second (a full turn takes 3 seconds). The rotation trajectories of magnetic particles were recorded at 20 Hz sampling frequency and 1 ms exposure time.

5.3.4. Monomer to catalyst ratio is estimated to be >10^7:1 in single polymer growth experiment

In the field of view (~79 × 59 μm^2), the average number of G2-loaded magnetic particles is less than 100. The radius of each magnetic particle is ~ 1μm (**Fig. S6**), so the total surface area of 100 magnetic particles is ~1.3×10^7 nm^2. Assuming the surface of each particle is fully covered by a monolayer of G2 catalyst (an overestimate), the total number of G2 catalyst in the field of view is ~ 10^7 molecules, assuming each G2 is ~1 nm^2. The total volume of monomer solution within the field of view in the follow cell is ~4.7×10^5 μm^3, and the number of monomers of a 1 M solution in the field of view is ~2.8×10^{14} molecules. Therefore, the monomer to catalyst ratio in 1 M monomer solution should be > 10^7:1.

5.4. Analysis of the real-time extension trajectories

To extract the four parameters, jump length j, wait time τ, occurrence time t, slope s, and polymerization rate v for each wait-and-jump event in the extension-vs-time trajectories, we did the following:

(1) Smooth the original trajectory of a tethered particle using a forward-backward nonlinear filtering function that preserves step features (*58*) (**Fig. S14**), which helps identify the jumps.

(2) Manually pick the start and end points of every possible jump using the smoothed trajectory, and connect them by a straight line. We only choose jumps that are larger than ~10 nm, which is about our z precision in tracking. The identification of the jumps also gives the wait periods in between.

(3) Fit each waiting time period of the raw trajectory using a linear function, which intersects with the straight line of the jump (**Fig. S14** inset). The slope of the linear fit of the waiting period is s.

(4) j, τ and t are defined as in **Fig. S14** inset, based on the trajectory after linear fitting (red line in **Fig. S14**). j in nm (extension) is further converted to the number of subunits.

(5) If any jump length is smaller than the z noise level of the trajectory (~10 nm, varies in different trajectories), the jump will be removed.

(6) Repeat step (3) to (5) until all jump lengths are larger than the z noise level.

(7) For data analysis purpose, we only consider wait-and-jump events that occurred after completing the flow in of the monomer solution, indicated by the black triangle (**Fig. S14**). Any increase of extension during monomer flow

was not monitored experimentally, as the solution flow pushed down the particle toward the coverslip surface.

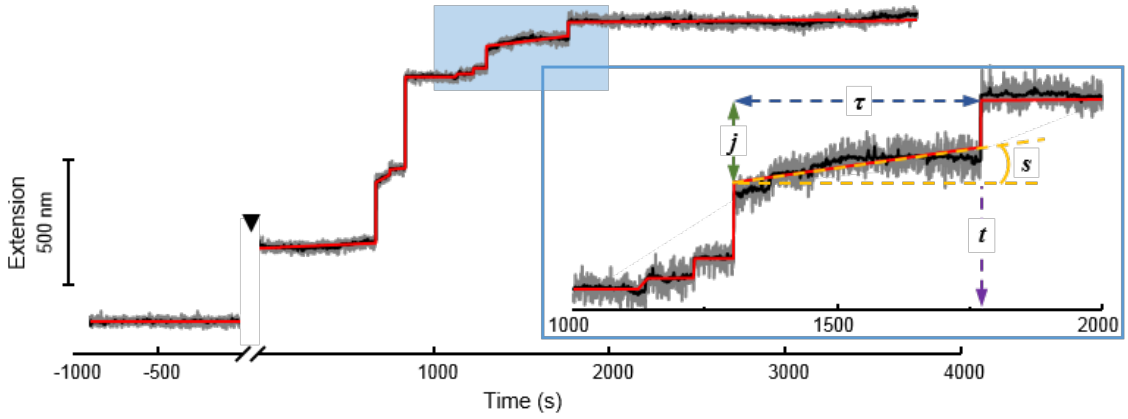

Fig. S14. Growth trajectory smoothing and linear fitting. Original extension-vs-time growth trajectory of a tethered particle during ROMP (grey), the smoothed trajectory using a nonlinear forward-backward filtering (black), and the linear fittings of the jump and waiting segments (red). Solid black triangle marks the monomer addition at ~0 seconds, and the break in the *x*-axis was the monomer flow time, in which the extension was not measured. Inset: zoom-in of the blue area of the growth trajectory, and the definition of j, τ, s and t.

For individual polymer growth trajectory with N wait-and-jump events, the following terms are defined to represent the properties of the entire trajectory:

(1) Average jump length $\langle j \rangle = \sum j / N$.

(2) Average waiting time $\langle \tau \rangle = \sum \tau / N$.

(3) Average waiting-time-slope of each polymer S = (total extension expansion during all waiting times)/(total waiting time) = $\sum (s \times \tau) / \sum \tau$

(4) Average polymerization rate of each polymer V = (total growth length)/(total growth time) = $\sum j / \sum \tau$

5.5. Control experiments

5.5.1. At 20 Hz time resolution, real-time single-polymer growth still exhibits wait-and-jump steps

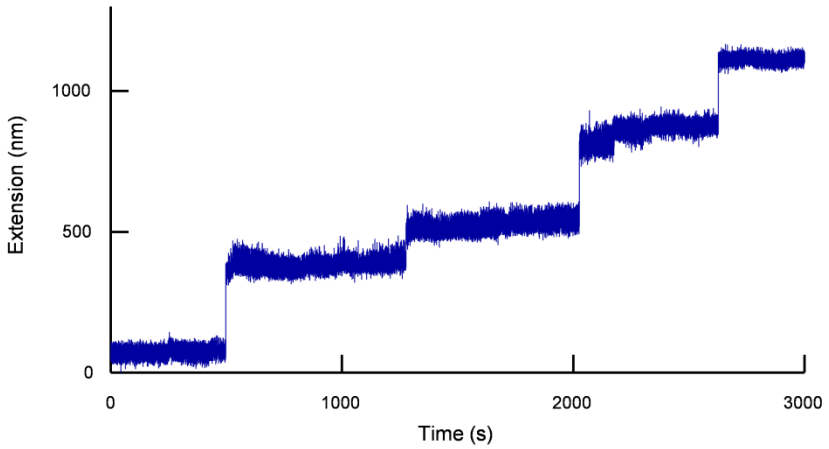

Fig. S15. A real-time extension vs. time trajectory recorded at 20 Hz for a single polynorbornene, in 1 M norbornene under 17 pN magnetic force in toluene. Norbornene monomer is addition at 0 seconds. All jump events happen within a single frame (0.05 seconds).

5.5.2. Multiple-tethered magnetic particles can be readily identified by rotational manipulations

The rotation and real-time extension growth behavior of a multi-tethered particle is shown in **Fig. S16**. Rather than being an approximate circular pattern, the trajectory of the *xy* center position of multi-tethered particle shows asymmetric and irregular patterns during external magnets rotation (**Fig. S16A**). Also, the periodicity of its *x* and

y fluctuations is different from the rotational periodicity of the magnets (**Error! eference source not found.**). Both reflect that a multi-tethered magnetic particle jerks back to its original position before making a circular procession pattern on the *xy* plane, due to the accumulated torque during magnetic rotation. Furthermore, the extension of the multi-tethered particle does not increase significantly after monomer addition (**Fig. S16C**).

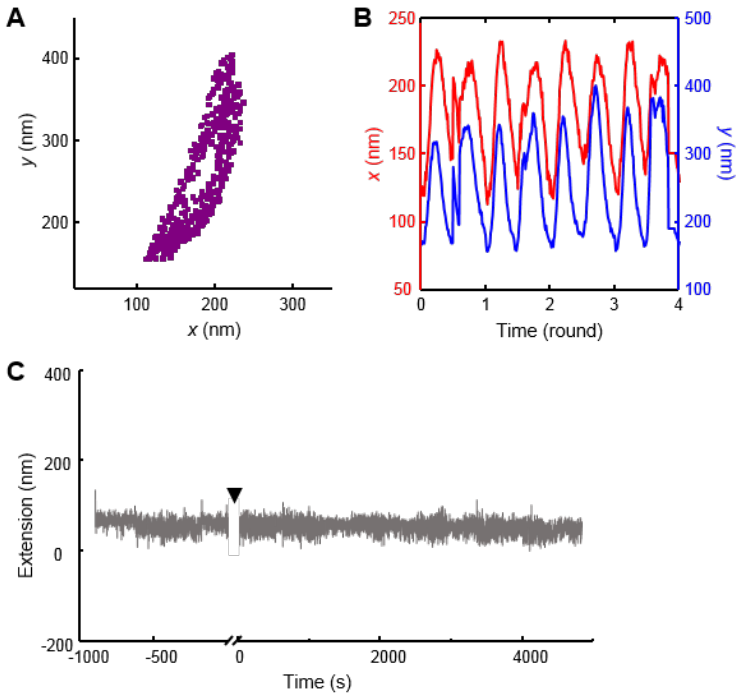

Fig. S16. (**A**) *xy* center position of a multi-tethered particle during magnets rotation before polynorbornene growth. (**B**) *x* and *y* center position of the multi-tethered magnetic particle vs time in **A**. The particle returns to the original position twice within each round of external magnets rotation. (**C**) Extension vs. time trajectory of the multi-tethered particle in **A** in 1 M norbornene and 17 pN force. Solid black triangle marks the monomer addition at ~0 seconds, and the break in the *x*-axis was the monomer flow time, in which the extension was not measured. The extension of the multi-tethered

particle does not increase significantly after monomer addition.

5.5.3. The wait-and-jump behavior of single polymer growth is still observed when the G2 catalyst is immobilized on the glass coverslip instead of the magnetic particle

To show that the wait-and-jump behavior in the extension-vs-time trajectory of single polymer growth is not related to polymer-particle surface interactions, we switched the tethering positions of the G2 catalyst and initial polynorbornene linker. G2 was immobilized on the glass coverslip and initial polynorbornene linker was grown on the silica-coated magnetic particle, following the same procedures in Section 5.2.3. In this configuration, the position for monomer incorporation is on the surface of glass coverslip, so that the newly incorporated polymer chain cannot wrap around the particle, which is pulled upward by the magnetic force. A real-time polynorbornene growth trace in 1 M norbornene and 17 pN force is shown in **Fig. S17**, in which the wait-and-jump behavior still exists.

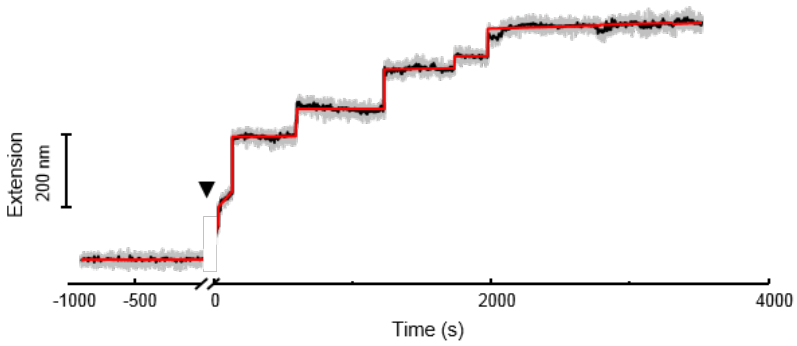

Fig. S17. Real-time extension vs. time trajectory for a single polynorbornene with the G2 catalyst immobilized on glass, in 1 M norbornene under 17 pN magnetic forces in toluene. Solid black triangle marks the monomer addition at ~0 seconds. Grey: Original

extension-vs-time growth trajectory; Black: smoothed trajectory using a nonlinear forward-backward filtering; Red: linear fittings of the jump and waiting segments.

5.5.4. Relaxing-stretching of single polymer tether after real-time growth produces WLC behaviors and no stepwise extensions

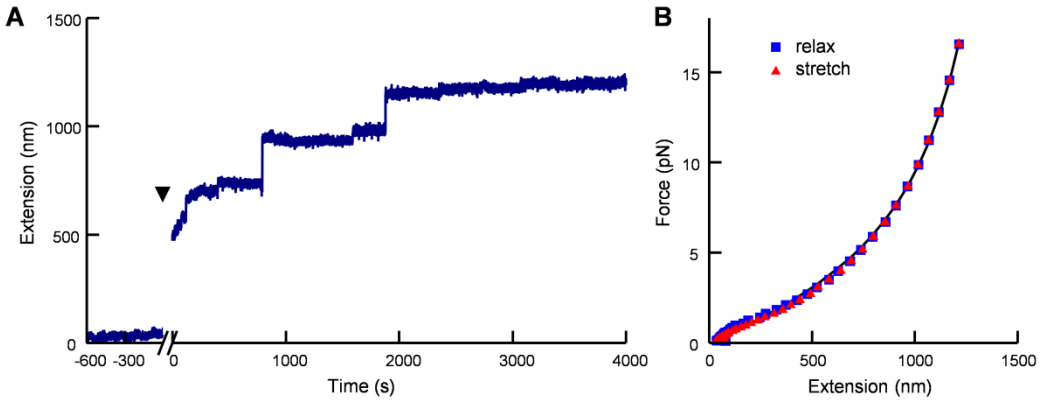

Fig. S18. (**A**) Real-time extension vs. time trajectory for a single polynorbornene in 1 M norbornene under 17 pN magnetic force in toluene. Solid black triangle marks the monomer addition at ~0 seconds. (**B**) Force-extension curves of the polymer grown in A after polymerization is stopped. The polymer was first relaxed by decreasing the magnetic force from ~17 pN to 0 pN (blue squares), and then stretched by increasing the magnetic force back to ~17 pN (red triangles). The stretching curve overlaps perfectly with the relaxing curve, without any discrete jumps or shortening of extension. Black curve is the worm-like chain model fitting, which gives a persistent length of 0.69 ± 0.02 nm.

5.5.5. High catalyst density on the magnetic particle diminishes the occurrence of wait-and-jump steps

With high catalyst density on the surface of magnetic particles, the extension-vs-time trajectory of a single polymer during growth became more continuous, in which the wait-and-jump behavior occurs much less (**Fig. S19A**). The high catalyst density leads to many polymer molecules growing on the same particle, one of which is tethered between the particle and the coverslip. Consequently, the inter-chain interactions among the different polymer molecules on the same particle likely interfere significantly with the intra-chain interactions within the tethered polymer molecule, thus inhibiting hairball formation or leading to much smaller hairballs, for which the jump length from hairball unraveling is below our measurement limit (~10 nm for a particle tethered to a flexible polymer) and the waiting time could be much shorter as well. In these cases, single polymer tether is still clear from the circular procession pattern of the magnetic particle on the *xy* plane during the rotation of external magnets after growth (**Fig. S19B**).

Furthermore, for these high-catalyst-density cases, after the completion of the polymerization reaction, the subsequent force-extension measurement gives an *apparent* extension that is much shorter than the extension increase measured during real-time growth. For example, for the single-polymer in **Fig. S19A**, the extension increased by ~984 nm at 17 pN over the course of growth, but upon lowering the force while measuring the force-extension curve in **Fig. S19C** after the polymerization is completed, the apparent extension is merely ~300 nm. We believe this apparent short extension is because the high catalyst density on the particle led to the formation of a thick polymer layer around the particle (besides the tether single polymer; **Fig. S19D**,

left), and upon lowering the force, this thick layer of polymer prevents the particle to return to the original *z* position at the start of the polymerization reaction (**Fig. S19D**, right), as compared with when the catalyst loading is low and the sparse polymers on the particle do not prevent the approaching of the particle to the coverslip surface (**Fig. S19E**).

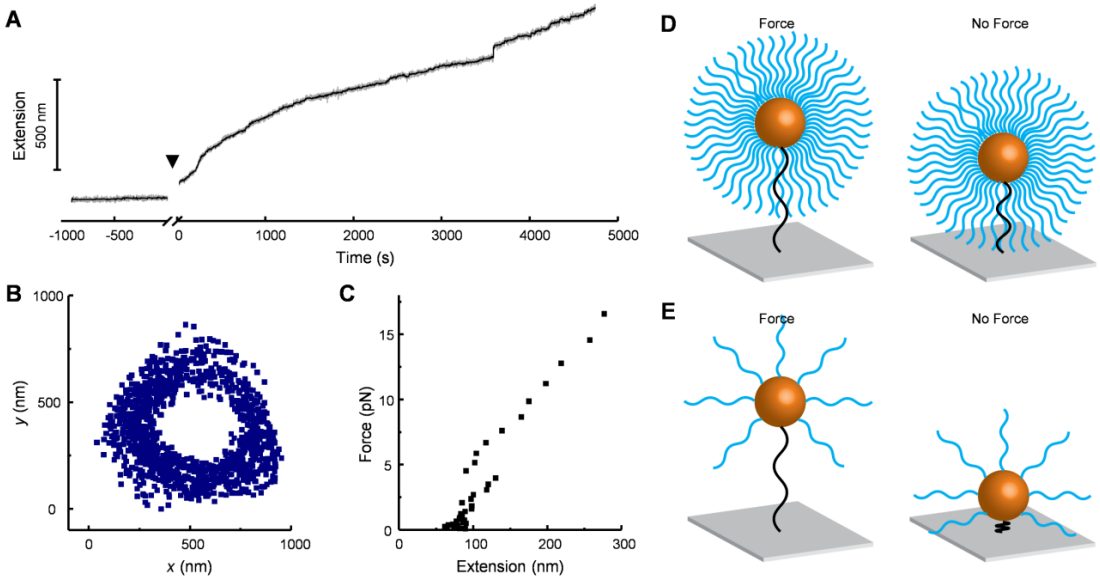

Fig. S19. (**A**) Real-time extension vs. time trajectory for a single polynorbornene under high G2 catalyst density on the magnetic particle in 1 M norbornene under 17 pN magnetic force in toluene. Solid black triangle marks the monomer addition at ~0 seconds. Merely one jump is clearly observed at ~3600 s, while the rest of trajectory shows more of a continuous increase behavior. Grey: Original extension-vs-time growth trajectory; black: smoothed trajectory using a nonlinear forward-backward filtering. (**B**) Trajectory of *xy* center position of the tethered particle in **A** during magnets rotation after polymer growth, indicating that it is single-polymer tethered. (**C**) Force-extension curve of the polynorbornene in **A** after the completion of the growth. The extension

between the highest and lowest force here is ~300 nm, much smaller than the increase of extension during polymer growth in **A**, consistent with that the magnetic particle is coated with a thick polymer layer due to high G2 catalyst density on the magnetic particle surface. (**D**) Illustration of force-extension behavior with high G2 catalyst density on the magnetic particle, as shown in **C**. The change of extension does not reflect the actual length of the polymer tether (black), but severely affected by the thickness of polymer cushion formed around the magnetic particle (blue). (**E**) Illustration of force-extension behavior with low G2 catalyst density on magnetic particle.

5.5.6. Intermolecular chain transfer, PCy_3 ligand rebinding, and interactions with the glass or magnetic particle surface are *not* the reasons for the wait-and-jump steps

Beside hairball formation, a few other process could potentially explain the wait-and-jump behavior of single polymer growth. Here we present the evidences and rationales to rule them out.

5.5.6.1. Intermolecular chain transfer is not the reason.

A polymer molecule growing on the same particle proximate to the tethered polymer could potentially undergo chain transfer reaction with the tethered polymer, lead to a sudden increase in extension. However, it should not be the reason because:

(1) Inter-molecular chain-transfer cannot explain the presence of the waiting period. If chain-transfer is the dominant contributor to the sudden extension increase,

the extension before the chain-transfer reaction should show a steady increase from continual polymerization.

(2) Chain transfer reaction would lead to cleavage of the tethered polymer with a 50% probability. To have 5 chain transfer reactions while preserving the tether, the probability is <4%. Experimentally, the average number of jumps is ~5 per polymer, i.e., 50% of polymers have more than 5 jumps, an order of magnitude higher than 4%.

(3) Chain transfer reaction should occur more frequently at higher catalyst density on the particle, in which polymer molecules are closer. On the contrary, we observe fewer jumps when the catalyst density is high (**Fig. S19A**).

5.5.6.2. PCy_3 ligand (or another inhibiting ligand) rebinding is not the reason.

PCy_3 ligand rebinding to the Ru center of the G2 catalyst could potentially pause the polymerization reaction, leading to a waiting period. However, this contribution to our experimentally observed wait-and-jump steps should be insignificant because:

(1) The sudden jump after the waiting period should then correspond to polymerization reaction after PCy_3 dissociation. The sudden jumps are up to ~10^3 nanometers in length (i.e., ~10^3 monomers) and are instantaneous within our shortest time resolution (0.05 s), which are too fast compared to the averaged ROMP rates for individual polymers (~10^0 s^{-1}, e.g., **Fig. 3G**).

(2) Adding 1 to 10 mM PCy_3 (10^2 -10^3 times less than the monomer concentration, but 10^4 -10^5 times larger than the estimated catalyst amount) to the reaction solution did not cause any noticeable differences in the step-wise extensions, supporting that PCy_3 rebinding is not the reason for the step-wise extension increases.

(3) The initiation of the G2 catalyst upon tethering the particle to the surface involves the dissociation of the PCy_3 ligand (*59*), so the maximum possible concentration of free PCy_3 in solution is about the concentration of G2 catalyst on the magnetic particles that we initially introduced (<100 nM). Additionally, the flow cell was flushed by both solvent and monomer solution after the tethering reaction, during which the PCy_3 ligand unbinds, so free PCy_3 ligand should be negligible.

(4) After G2 initiation and monomer addition, any residual PCy_3 ligands and the monomers bind competitively to Ru. The concentration ratio of monomer (1 M) to PCy_3 is > 10^7:1. With similar binding rate constants (*59*), the binding rate ratio of monomer to PCy_3 is > 10^7:1. Assuming the binding rate of norbornene to Ru is ~100 s^{-1}, the binding rate of PCy_3 would be <1×10^{-5} s^{-1}. Meanwhile, the unbinding rate of PCy_3 from Ru is expected to be ~5×10^{-4} s^{-1} (*59*).

If the waiting period were to correspond to G2 inactive state (PCy_3 bound) and jump were to correspond to G2 active state (PCy_3 unbound), the waiting period should be on average equal to the inverse of the unbinding rate of PCy_3, i.e., ~2000 s, about 10 times longer than the average waiting times we observed; the duration of jump should be on average equal to the inverse of the binding

rate, i.e., $>10^5$ s, whereas the experimental observed jumps are instantaneous within our shortest time resolution (0.05 s).Therefore, wait-and-jump is not caused by PCy_3 binding and unbinding.

(5) If PCy_3 were bound to Ru during the waiting period, G2 catalyst should be inactive and the extension of polymer tether should stay constant during the waiting periods. However, 75% of the waiting periods have a clear positive slope (e.g., **Fig. 3C**), indicating PCy_3 rebinding should not be the reason for the waiting period.

(6) Higher concentration of G2 catalyst should give higher concentration of free PCy_3. If wait-and-jump were due to PCy_3 binding and unbinding, waiting periods should occur more frequently at higher G2 loading. To the contrary, continuous growth behavior was observed at high G2 loading (**Fig. S19**), where wait-and-jump behavior almost disappeared.

(7) Previous single molecule fluorescence experiment on catalyst initiation also showed that at the low catalyst concentration condition, the ligand does not re-bind to the metal center of the catalyst immobilized on surface after the ligand falls off during initiation (*60*).

Instead of PCy_3, if it were to be another un-identified ligand that could potentially bind to the Ru center of the G2 catalyst and inhibit reaction, the above rationales (1), (4), and (5) also apply to argue against this possibility.

5.5.6.3. Polymer-surface interactions are not the reason.

The observation that the wait-and-jump behaviors persist regardless of the G2

catalyst on the particle or on the coverslip indicates that the wait-and-jump behaviors are neither specific to where the catalyst is immobilized, nor to which side the new monomers are incorporated (**Fig. S17**). We also performed repeated stretching-releasing cycles after the polymerization is completed, during which the tethered single polymer havs ample opportunities to interact with the surfaces of both the magnetic particle and the coverslip. In all these, stretching-releasing is reversible without any sudden jumps in extension (**Fig. S18B**). Therefore, possible interactions of the polymer with the magnetic particle or the coverslip do not give rise to the wait-and-jump behaviors.

5.6. Simulation Methods and Results

5.6.1. Force Fields

All systems were modeled using TraPPE-UA (united atom) force field (*50*, *61*, *62*). The non-bonded interactions between united atoms followed the pairwise-additive Lennard-Jones (LJ) potential:

$$U_{nonbonded} = 4\varepsilon_{ij}\left[\left(\frac{\sigma_{ij}}{r_{ij}}\right)^{12} - \left(\frac{\sigma_{ij}}{r_{ij}}\right)^{6}\right], r_{ij} < r_c \qquad \textbf{Eqn. S9}$$

The unlike LJ interactions are determined using Lorentz-Berthelot combining rules: $\sigma_{ij} = \frac{1}{2}(\sigma_{ii} + \sigma_{jj})$ and $\varepsilon_{ij} = (\varepsilon_{ii}\varepsilon_{jj})^{\frac{1}{2}}$. The LJ parameters used in our polynorbornene and polycyclooctene models are tabulated in **Table S1**.

Table S1. Lennard-Jones parameters for the TraPPE-UA force field.

(pseudo) atom	σ ( )	ε (kcal/mol)
CH (sp^2)	3.730	0.094
CH_2(sp^3)	3.950	0.092
CH (sp^3)	4.650	0.020
CH_3(sp^3)	3.750	0.196

The interactions between bonded pairs of united atoms are described by the harmonic potential:

$$U_{bond}(r) = \frac{k_r}{2}(r - r_0)^2 \qquad \textbf{Eqn. S10}$$

For all bond types, the k_r constant is 240.02 $\text{kcal} \cdot \text{mol}^{-1} \cdot \text{nm}^{-2}$ based on the PYS united atom force field described by Paul et al.(*63*), with equilibrium bond length of 0.154 nm for CH_x-CH_y and 0.133 for CH=CH.

Atoms separated by two bonds forming angle θ interact via a harmonic bending potential, with parameter summarized in **Table S2**:

$$U_{bond}(\theta) = \frac{k_\theta}{2}(\theta - \theta_0)^2 \qquad \textbf{Eqn. S11}$$

Table S2. Equilibrium bond angles and force constants for the TraPPE-UA force field.

Bend type	θ_0 (°)	k_θ (kcal/mol)
$CH_x(sp^2)$=$CH(sp^2)$-CH_y	119.7	140.84
CH_x- $CH_2(sp^3)$-CH_y	114.0	125.00
CH_x-$CH(sp^3)$-CH_y	112.0	125.00

The torsional angle (ϕ) potential follows the OPLS-UA force field dihedral function (**Table S3**):

$$U_{tors}(\phi) = c_0 + c_1[1 + \cos(\phi)] + c_2[1 - \cos(2\phi)] + c_3[1 + \cos(3\phi)] \qquad \textbf{Eqn. S12}$$

Table S3. Torsional potential parameters for the TraPPE-UA force field.

	c_i (kcal/mol)			
Torsion	i = 0	1	2	3
CH_x-(CH_2)-(CH_2)-CH_y	0	0.710	-0.136	1.583
CH_x-(CH_2)-(CH)=CH_y	1.377	0.173	-0.220	-0.564

A harmonic torsional potential is used for *trans*- and *cis*- dihedral interactions (**Table S4):**

$$U_{tors}(\phi) = \frac{d_0}{2}(\phi - \phi_0)^2 \qquad \textbf{Eqn. S13}$$

Table S1. Torsional potential parameters for *trans*- and *cis*- dihedral interactions.

Torsion	ϕ (°)	d_0 (kcal/mol)
CH_x-(CH)=(CH)-CH_y (*cis*)	180.0	24.8
CH_x-(CH)=(CH)-CH_y (*trans*)	0.0	26.8

All united atoms in these systems have no partial change.

5.6.2. Hairball formation driven by torsional strain

To build a polynorbornene model, we linearly connected monomer configurations chosen randomly and with equal probability from the four possible types (*meso-cis, meso-trans, racemo-cis* and *racemo-trans*) (*64*). Our choices for the initial torsional angles are marked in **Fig. S20** and **Fig. S21**. The resulting linear chain has 146 monomers with a contour length of nearly 100 nm. To build a polycyclooctene chain, we used 100 monomers to also reach a ~100 nm contour length by connecting *cis* or *trans* monomer configurations chosen randomly with equal probability. To mimic how the torsional strain production may be accumulated in the experiment, we kept the two

ends of the polymer fixed, while allowing the bending angles and bonds to equilibrate, but keeping the initial dihedral angles unequilibrated (i.e., strained). After freeing up one end, the chain quickly collapsed and formed a hairball, which was then equilibrated for another 2 ns.

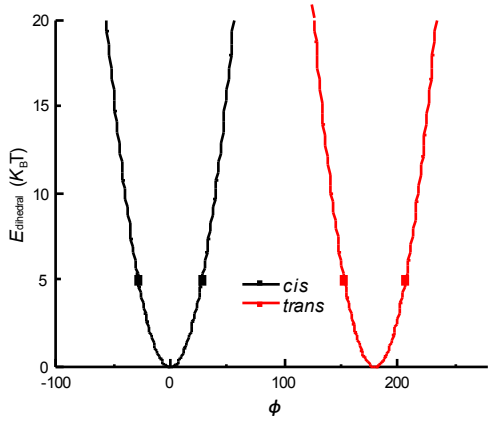

Fig. S20. Torsional angle potential for CH_x-CH=CH-CH_y (*cis*) and CH_x-CH=CH-CH_y (*trans*) in polynorbornene as per **Eqn. S13** with initial torsional angle shown in black and red squares, respectively.

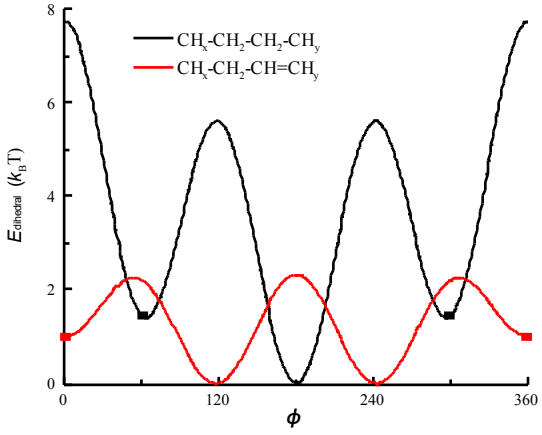

Fig. S21. Torsional angle potential for CH_x-CH_2-CH_2-CH_y and CH_x-CH_2-CH=CH_y in polynorbornene as per **Eqn. S12** with initial torsional angles marked by black and red

squares, respectively.

During the pulling process, the torsional angle energy and bonded potential remain unchanged (see **Fig. 2F** and **Fig. S22**), while the non-bonded pair contacts that were formed during collapsing (**Fig. 2D**) are broken as the chain unravels (**Fig. 2G**).

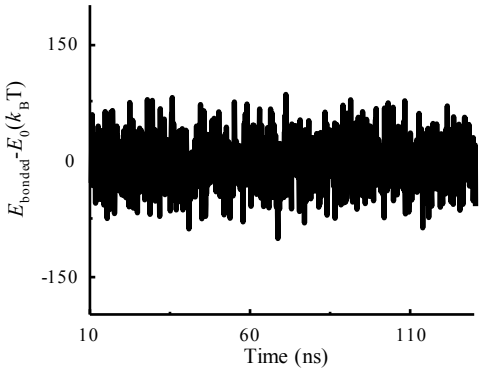

Fig. S22. Time evolution of the bonded potential (including bond stretching, bending angle and dihedral potential) during a polynorbornene hairball pulling simulation at 20 pN force.

5.6.3. Implicit solvent and effective temperature

All simulations were performed using the molecular dynamics simulator LAMMPS (*65*) via the leapfrog algorithm with a time step of 1 fs. The cubic box dimensions were approximately 500 nm. Given the large sizes of our systems, it would be impractical to use solvent-explicit simulations at T = 300 K. To approximate good solvent conditions in our solvent-implicit simulations, we identified the "effective" temperature at which the solvent-implicit *N*-mer polynorbornene chain has an root-mean-square of radius of gyration, $\langle R_g^2 \rangle^{1/2}$, *vs*. N^{ν} curve with the expected scaling

exponent v of ~3/5.[7] The results of these single-chain simulations are shown in **Fig. S23**, which show that the good-solvent slope is approached at T = 500 K. Accordingly, all the simulation results reported in the main text and the SI were performed at T = 500 K. The scaling relations $\langle R_g^2 \rangle^{1/2} \sim N^v$ for polycyclooctene are shown in **Fig. S24**, the simulations reported for polycyclooctene were performed at T = 500 K.

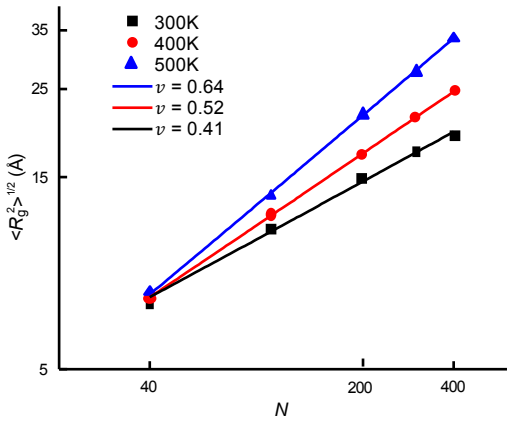

Fig. S23. Root-mean-square of radius of gyration $\langle R_g^2 \rangle^{1/2}$ vs. N for the N-mer polynorbornene chain in vacuum simulated at T = 300 K, 400 K and 500 K (symbols). The solid lines are the power-regression best fits to the data.

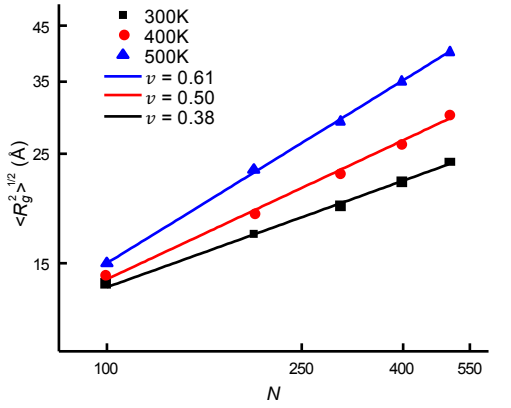

Fig. S24. Root-mean-square of radius of gyration $\langle R_g^2 \rangle^{1/2}$ vs. N for the N-mer

polycyclooctene chain in vacuum simulated at T = 300 K, 400 K and 500 K (symbols). The solid lines are the power-regression best fits to the data.

5.6.4. Analysis of waiting and jumping behavior in the simulated extension trajectory

Key quantities to extract from the end-to-end chain extension vs. time plots generated by the force-driven simulations are the waiting time τ and the jump length j. The jump length j is the extension difference between the start of the pulling and the maximum average length after the pulling unravels the hairball. In our simulation, since the polymer chain is fixed in length, j is only dependent on the pulling force, which determines the maximum average length after hairball unraveling.

To extract out the waiting time τ from the pulling simulation trajectory, we defined another time parameter, the jumping time t, so that $\tau + t$ is the total time needed to reach the maximum average extension for the first time; this $\tau + t$ is made up of a number n_p of successive points (i=1,2,..,n_p). Since the τ and t periods are defined as successive regions in the curve of slow and fast growth (i.e., small and large slopes), they are found by identifying a point "k" such that separate linear regressions, one for points [1,2,..k] and the other for points [k+1,k+2,…,n_p] minimize the total sum of squared deviations from the simulation data. Since the k point is the intersection of both linear fits, it defines the beginning of a jumping event, so that τ is the time between points 1 and k while t is the time between points k+1 and n_p.

Fig. S25A shows that a higher pulling force shortens the waiting time for the same hairball. After the hairball unravels, the polymer extensional behavior follows the

wormlike chain (WLC) model (**Fig. S25B**), with a backbone persistence length of ~0.67 nm consistent with the experimental data (~0.71 nm; Fig. 1D inset).

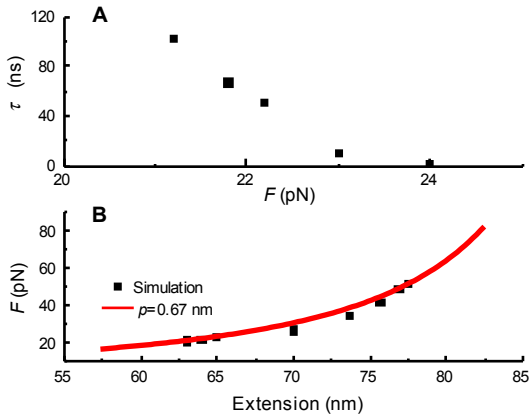

Fig. S25. (**A**) Waiting time τ vs. force applied to the polynorbornene hairball. (**B**) WLC-model fit of the force vs. extension plot from the unraveled polymer, with a backbone persistence length of p=0.67 nm.

5.6.5. Re-pulling of unraveled polynorbornene chain does not produce stepwise jumps

After the hairball unraveled, we freed up one chain-end and equilibrated the chain for 2 ns; we then applied the same constant-force on one end and monitored the change in extension over time (**Fig. S26A**). The relaxed chain did not form an entangled hairball and, upon applying a pulling force, no clear waiting period was observed in the extension.

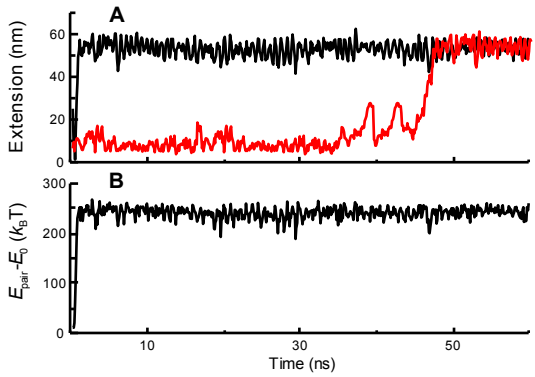

Fig. S26. Time evolution of (**A**) chain extension and (**B**) non-bonded pair potential of a pre-unraveled polynorbornene chain during the re-pulling simulations at 22 pN force (black lines). The 22 pN-force extension vs. time curve for the hairball pulling simulation is shown by the red line in **A**.

5.6.6. Hybrid polynorbornene chain still forms hairball

We conducted simulations to mimic the conjectured experimental situation, where one half of the polymer configuration consisted of a relaxed part, while the other half accumulated non-equilibrium torsional strain (**Fig. S27A** with t=0 ns). Under such conditions, the hairball still formed as the chain collapsed (**Fig. S27A** with t=10 ns, and **B-D**), and exhibited the distinctive wait-and-jump behavior upon pulling (**Fig. S27E-G**). We also observed that the hairball "shifted" around along the chain backbone before the unraveling occurred.

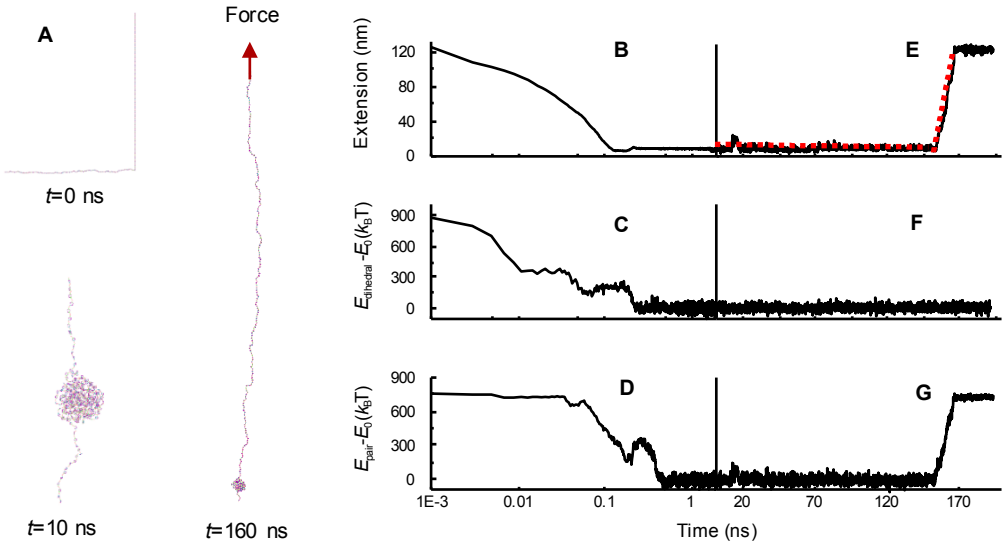

Fig. S27. Simulation results for hybrid polynorbornene chain. (**A**) Structures of a hybrid 292-mer polynorbornene chain showing a linear configuration at t=0 ns, a collapsed hairball at t=10 ns, and a partially unraveled chain midway the jumping event at t=160 ns, with one chain-end tethered and the other chain-end pulled with constant force. (**B-D**) Time evolution of end-to-end extension (**B**), dihedral potential (**C**) and non-bonded pair potential (**D**) of the chain collapsing from a linear configuration into a hairball. (**E-G**) Subsequent evolutions upon applying a constant 22 pN pulling force starting at 8 ns. Linear regression fits to the waiting and jumping portions of **E** are shown as red dotted lines.

5.6.7. Polycyclooctene hairball formation and unraveling

We conducted simulations for a polycyclooctene chain at T = 500K using the simulation protocols described in previous sections. After freeing up one end, the chain collapsed into a hairball-like configuration as depicted in **Fig. S28**. During the hairball pulling simulations, we observed wait-and-jump behaviors, similar to those observed

for the polynorbornene chain (**Fig. 1C**).

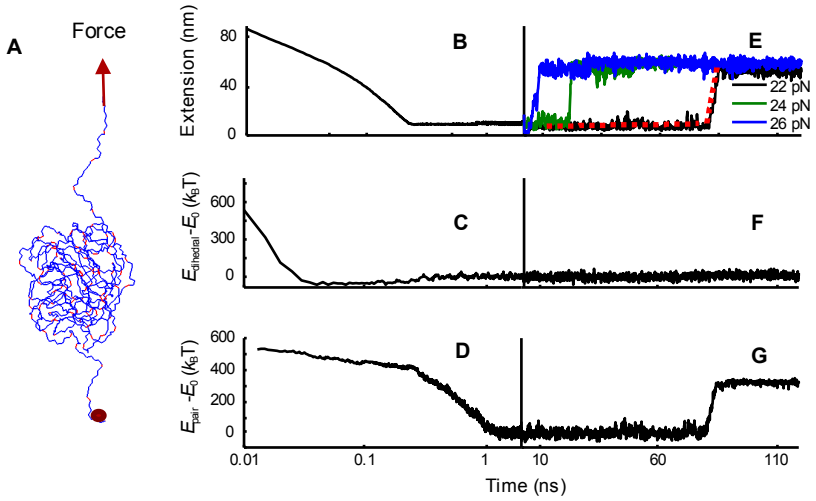

Fig. S28. Simulation results for polycyclooctene. (**A**) Structure of a hairball at 2 ns from a collapsed 100-mer polycyclooctene chain with one chain-end tethered and the other chain-end pulled by a constant force. (**B-D**) Time evolution of end-to-end extension (**B**), dihedral potential (**C**) and non-bonded pair potential (**D**) of a 100-mer polycyclooctene chain collapsing from a linear configuration into a hairball. (**E-G**) Subsequent evolutions upon applying a constant pulling force starting at 8 ns. **E** shows results from three different applied forces. Linear regression fits to the waiting and jumping portions of the 22 pN pulling curve are shown as red dotted lines. **F** and **G** correspond to 22 pN only.

Fig. S29A shows that, akin to the polynorbornene chain behavior, a higher pulling force shortens the waiting time for the same hairball. After the hairball unraveled, the polymer extension behavior also follows the WLC model (**Fig. S29B**), with a backbone persistence length of ~0.75 nm, within the error bar of the experimental result of ~0.88 ± 0.12 nm (**Fig. S38M**).

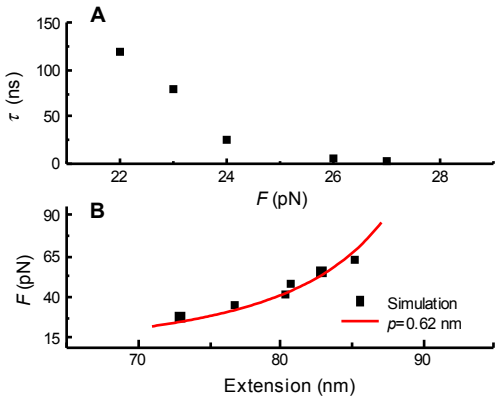

Fig. S29. (**A**) Waiting time vs. force applied to the polycyclooctene hairball. (**B**) WLC model fits to the simulation data of force vs. extension from the unraveled chain is shown as red line, with a backbone persistence length of p=0.62 nm.

5.6.8. Approximate effect of solvent quality: hairball is more persistent in lower-quality solvent

We observed similar results for T = 350 K (representative of lower solvent-quality conditions) in terms of hairball formation and the presence of waiting and jumping behavior during forced extension (**Fig. S30A**). Our results show that waiting times become longer at lower temperatures for extensions under the same pulling force (**Fig. S30B**), consistent with the expectation that the hairball "collapsed" state would become more persistent in a lower-quality solvent.

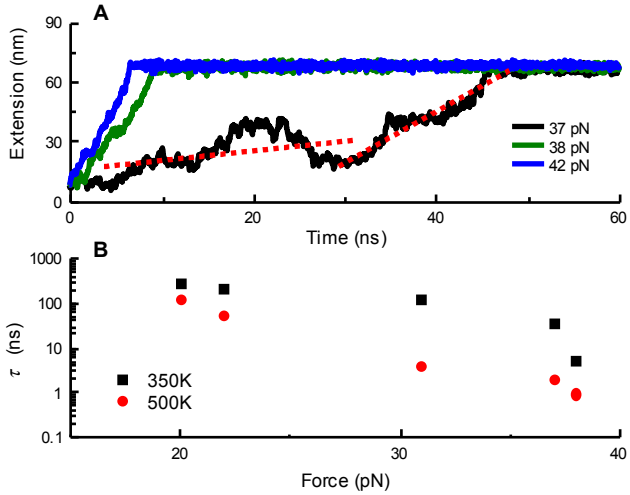

Fig. S30. (**A**) Time evolution of chain extension during polynorbornene hairball pulling simulations for different applied forces at T = 350 K. Linear regression fits to the waiting and jumping portions of the 37 pN-force extension vs. time curve are shown by red dotted lines. (**B**) Waiting time vs. force for hairball pulling simulations at T = 350 K and 500 K.

5.7. Additional results

5.7.1. Statistical analysis of wait-and-jump behaviors under additional reaction conditions.

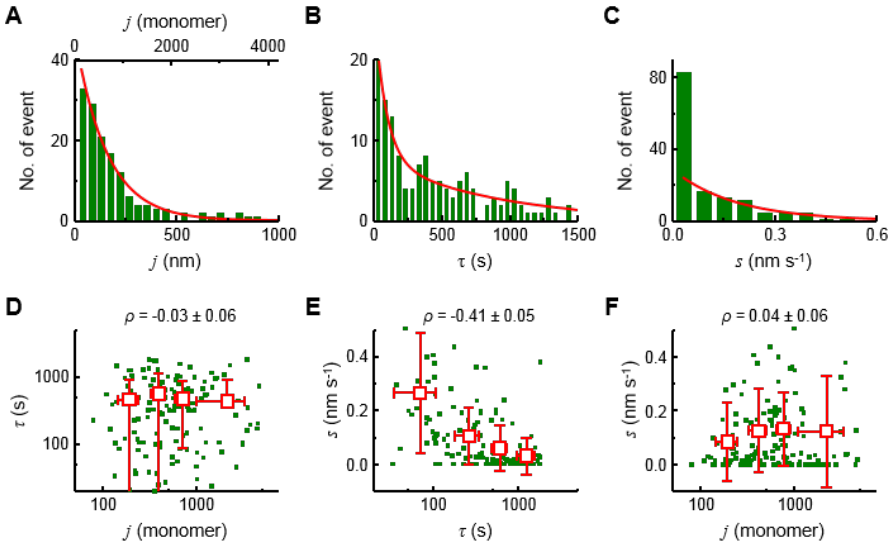

Fig. S31. Statistical properties of wait-and-jump behaviors of single polymer growths under 1 M norbornene and 4.5 pN force. **(A-C)** Histograms and exponential fits (red lines) of jump length j, waiting time τ, and waiting period slope s from 38 single polymers growth trajectories. The exponential fit in **C** does not include the first bin, where $s \sim 0$. **(D-F)** Correlation plots and Pearson's correlation coefficients between τ and j, τ and s, and j and s from 38 single polymers growth trajectories. Each solid black square is from one wait-and-jump event. Open red squares are averages from bins of equal number of events. x and y error bars are s.d.

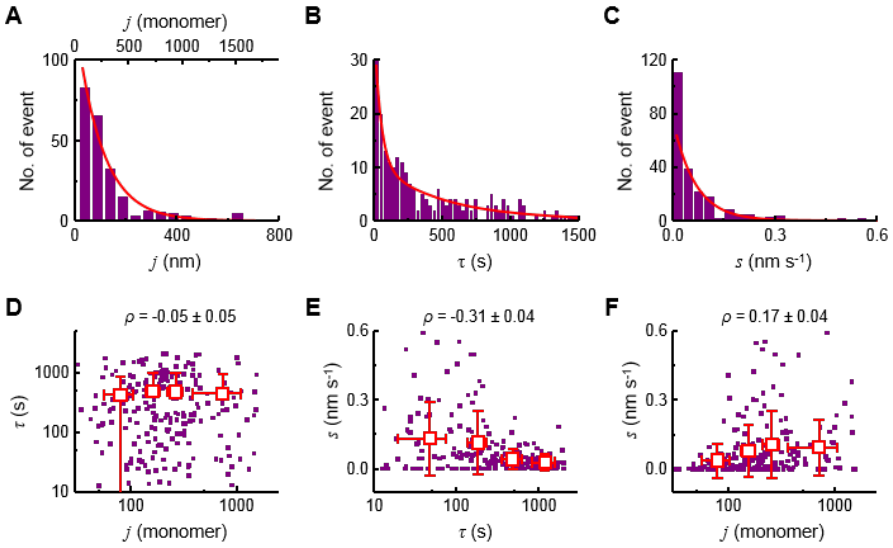

Fig. S32. Statistical properties of wait-and-jump behaviors of single polymer growths, as **Fig. S31**, but for 0.1 M norbornene and 17 pN force.

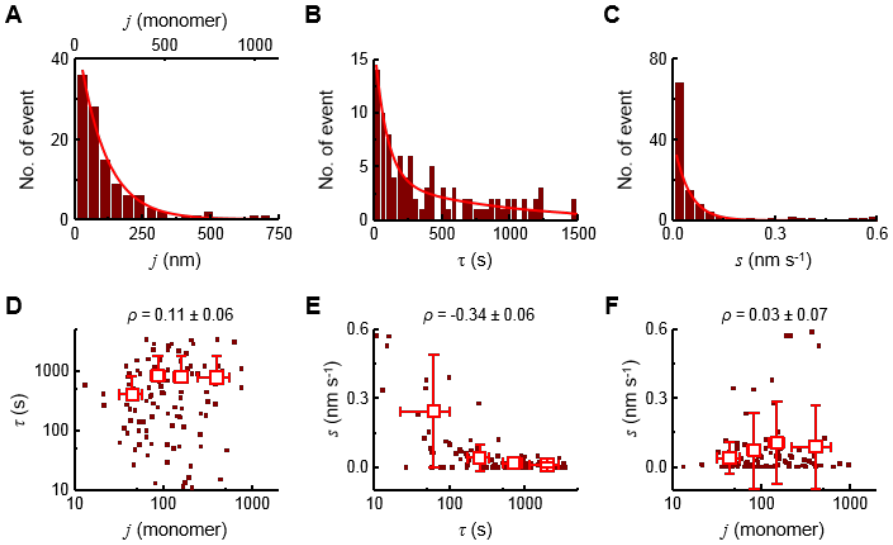

Fig. S33. Statistical properties of wait-and-jump behaviors of single polymer growths, as **Fig. S31**, but for 1 M *cis*-cyclooctene and 17 pN force.

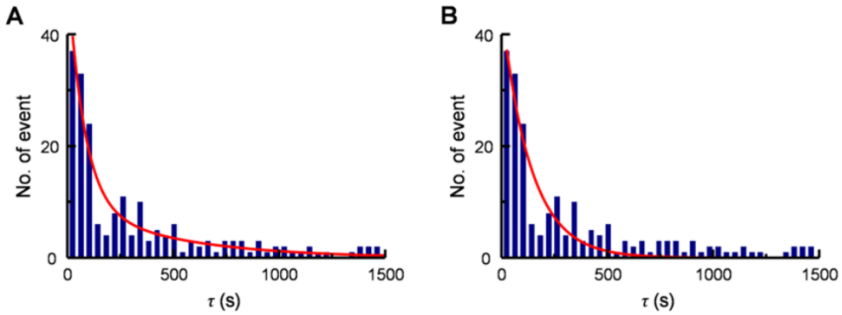

Fig. S34. Fitting of waiting time distribution from extension trajectories taken at 1M norbornene and 17 pN force by a double-exponential function (**A**) or a single-exponential function (**B**). It is clear that single exponential function does not fit the distribution well enough. For waiting time distributions under other experimental conditions, same multiexponential behaviors were observed.

5.7.2. The jump length and waiting time do not show temporal dependence over the course of polymerization reaction

The jump length and waiting time under 1 M norbornene and 17 pN force are plotted against the time *t* when they were observed in **Fig. S35A** and **B**. The observation time *t* is the end point of each waiting time where a jump occurs (**Fig. S14**). The jump length *j* does not show any discernable temporal dependence (**Fig. S35A**), indicating the size of the hairball does not depend on the existing length of a growing polymer.

The waiting time τ shows a strong positive correlation with observation time *t*, because of the following reasons:

(1) τ cannot be larger than *t*. The occurrence time *t* for the N^{th} wait-and-jump event is the sum of τ values of all *N* events. In τ-*t* correlation plot (**Fig. S35B**), the first τ of each growth trajectory falls on the diagonal of τ-*t* correlation plot, and all other points must be distributed below the diagonal.

(2) As the number of events increases, τ deviates from the diagonal. When the number of events is large enough, τ-t correlation plot should exhibit rise-and-flatten shape and the correlation coefficient should approach zero (see simulation result in **Fig. S35D**), if τ has no time-dependence. However, the average number of events is only 5 in our experiments, so that τ-t correlation plot is still at the rising region, due to insufficient number of observed events per single polymer growth.

We simulated trajectories that contain 5 sequential waiting times τ (5 is the average number of wait-and-jump events we observe in single-polymer growth trajectories), where each τ is generated from a random sampling of a single exponential distribution with average being 333 s, comparable to that observed experimentally (**Fig. 3B**). This simulation also shows a similar dependence of τ on t (**Fig. S35C**), even though the simulated τ's are all random. When τ has no time-dependence, the correlation coefficient between τ and t approaches zero as the number of events becomes large enough (**Fig. S35D**).

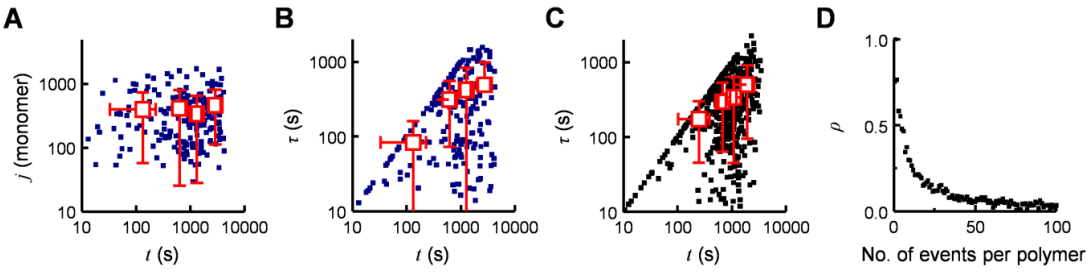

Fig. S35. The jump length j and waiting time do not show significant temporal dependence during polymer growth, using data from 1 M norbornene and 17 pN conditions. (**A**) j vs. t, the time when the jump was observed. (**B**) τ vs. t. (**C**) τ vs. t from

simulations. Each simulated trajectory contains 5 τ values, which are random numbers generated based on single exponential distribution with average being 333 s. Each solid square on the correlation plots is a single wait-and-jump event. Open red squares: binned and averaged results. x and y error bars are s.d. (**D**) Correlation coefficient ρ from the simulated results in **C** dependence on the number of wait-and-jump events per polymer growth trajectory, when τ has no temporal dependence.

5.7.3. Additional discussions on the lack of correlation between individual *j* and τ pairs

5.7.3.1. If the hairball size were directly coupled with hairball unraveling rate, *j* and τ should have strong positive correlation

From the real-time extension-vs-time trajectories, we observed that the jump length j and its prior waiting time τ have no significant correlation (e.g., $\rho = 0.08 \pm 0.05$ in **Fig. 3H**). We concluded from this observation that the unraveling rate of hairball, reflected by τ, is not directly coupled with the size of hairball, reflected by j. We rationalized this conclusion by that the global structural configuration of the hairball, which determines the unravelling rate, is not correlated strongly with the local structural configuration around the catalyst center, which determines the polymerization and the growth of the hairball.

To further support this conclusion, we performed simulations to show that if the unraveling rate of the hairball were to be directly correlated with the size of hairball, the jump length j and the waiting time τ should show positive correlation. The simulation was done as follows:

(1) Generate 1000 random values of j that follows a single exponential distribution with an exponential constant of 175 nm (**Fig. S36A**). The exponential distribution mimics the experimental determined distribution of j (e.g., **Fig. 3A**).

(2) Let the unraveling rate k of the hairball equal to j^{-1}, that is, the unraveling rate is *directly* related to the hairball size j.

(3) The waiting time τ, as the unraveling of a single hairball is a single-molecule event, should be probabilistic and sample a distribution $f(\tau)$, and $f(\tau) = k\exp(-k\tau)$, where k is the unraveling rate.

(4) While j is sampling the distribution in (**Fig. S37A**), each j gives a k, which gives the corresponding distribution of $f(\tau)$, from which τ samples randomly. The resulting distribution of τ is shown in **Fig. S37B**, which appears to be multiple exponential.

(5) The individual values of j and τ from this simulation shows strong positive correlation (**Fig. S37C**).

The distribution of Pearson's correlation coefficients between j and τ generated from 2000 simulations is shown in **Fig. S37D**. Clearly, j and τ have a strong positive correlation ($\rho = 0.58 \pm 0.03$). Therefore, if the hairball size and unraveling rate were to be directly correlated, a strongly positive correlation would be expected between j and τ. Consequently, the experimental observation that j and τ show no significant correlation indicates that the unraveling rate of hairball is not directly coupled with the size of hairball.

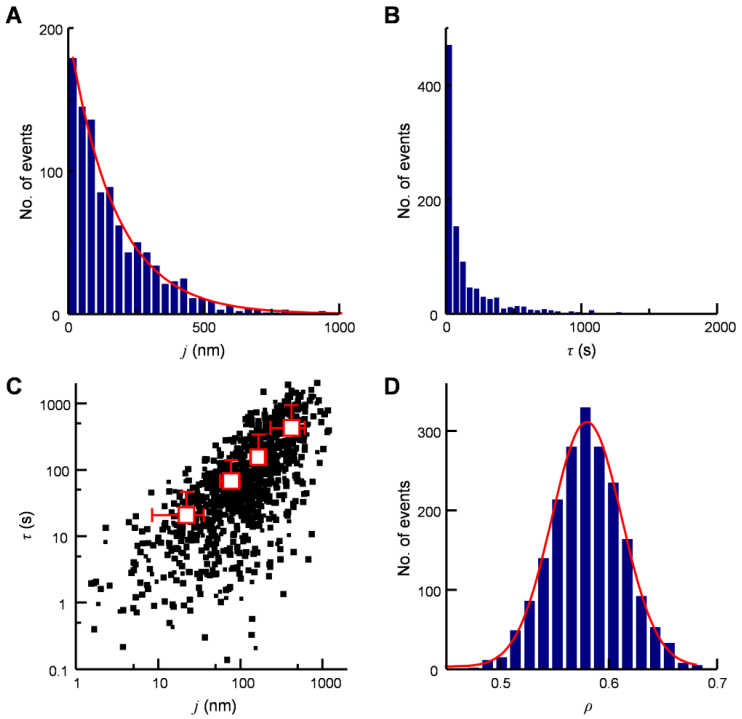

Fig. S36. Simulation of j-τ correlation, assuming the hairball size is directly coupled with hairball unraveling rate. (**A**) Assumed single exponential distribution of j, with the decay constant of 175 nm. (**B**) Distribution of τ following the simulation procedure. (**C**) Correlation plot between j values in (A) and τ values in (B). A strong positive correlation is observed. Each black dot is a pair of j and τ. The red squares are binned and averaged results. (**D**) Distribution of Pearson's correlation coefficient ρ between j and τ in 2000 simulations, ρ is 0.58 ± 0.03.

5.7.3.2. Other possibilities for the lack of j-τ correlation.

A few other potential reasons might explain the lack of j-τ correlation, and our experimental results cannot completely rule out these possibilities.

(1) Partial unraveling of hairball. If the hairball is partially unraveled, the jump

length j then does not reflect the total length of the polymer chain in the hairball that was formed during the prior waiting period. Under such conditions, if the fraction of the hairball that partially unravels changes from one event to another, the correlation between j and its prior τ is expected to be weak. Our simulations discussed in Section 5.6 show that the hairball unraveling is always complete, arguing against this possibility, but the simulations are done on polymers that are much shorter than the actual experimental systems and may not capture the entire features of hairball unraveling.

(2) Formation of multiple hairballs. During the waiting period, more than one hairball could potentially form and only one or some of them might unravel in the subsequent jump event. Under such conditions, j-τ correlation might be expected to be weak. However, multiple distinct hairballs are unlikely during a single waiting period, because if the first hairball is formed, there is little reason to form another distinct one without showing a wait period. One potential scenario for multiple hairball coexistence is that an early hairball might have partially unraveled and be now far from the catalyst site, while a new hairball starts forming near the catalyst.

5.7.4. Bulk NMR measurements show G2-catalyzed ROMP follows saturation kinetics with increasing monomer concentration under high monomer-to-catalyst ratios

In our single-polymer growth experiments, the average polymerization rate in 0.1 M norbornene and 17 pN force decreased only by ~29 % (**Fig. 3G**) compared with

that at 1 M norbornene, indicating the overall kinetics here is in the sub-linear regime, which appears in classic saturation kinetics in which the reactant has to form some type of complex with the catalyst before undergoing catalytic transformation such as in the G2-catalyzed ROMP (*59*).

To confirm that G2-catalyzed ROMP indeed follows saturation kinetics, we measured the ROMP rates catalyzed by G2 (10^{-5}M) as a function of norbornene monomer concentration using ^{1}H NMR to follow the appearance of polynorbornene over time (**Fig. S38A**). The measurement was in toluene (deuterated) at room temperature, as in our single-polymer growth measurements.

As expected, the ROMP rate exhibited saturation kinetics with increasing norbornene concentration (**Fig. S38B**), with an effective dissociation constant of norbornene from the catalyst of ~0.62 M (corresponding to 6.2×10^{4}:1 monomer to catalyst ratio). This dissociation constant is larger than what is expected from the single-polymer growth experiments (~0.1 M), likely because: (1) Monomer to catalyst ratio in single-polymer growth experiments (>10^{7}:1) is much higher than the bulk NMR measurements, so that the complexation of norbornene to the catalyst could be saturated at lower monomer concentration. (2) Modification of the NHC ligand on G2 might affect the binding affinity of monomers. (3) The dissociation constant represents an "effective" concentration of the monomer in complexation with the catalyst, and in the context of the hairball formation, this complexation is likely first with the hairball before the monomer transports through the hairball and reaches the Ru center of the catalyst. In this scenario, the hairball configuration would affect both the effective concentration of complexation with the monomer and the intra-hairball transport of the

monomer to the Ru center. This scenario is supported by the experimental observation that the polymerization rate of each polymer is correlated strongly with the hairball configuration (**Fig. 4B-D**). In free solution as in the bulk NMR kinetics measurements vs. in our single-polymer measurement where the polymer is tethered at two ends and being pulled, the microscopic configuration of the formed hairballs is expected to differ, which may lead to a difference in the effective dissociation constant of the monomer in the saturation kinetics.

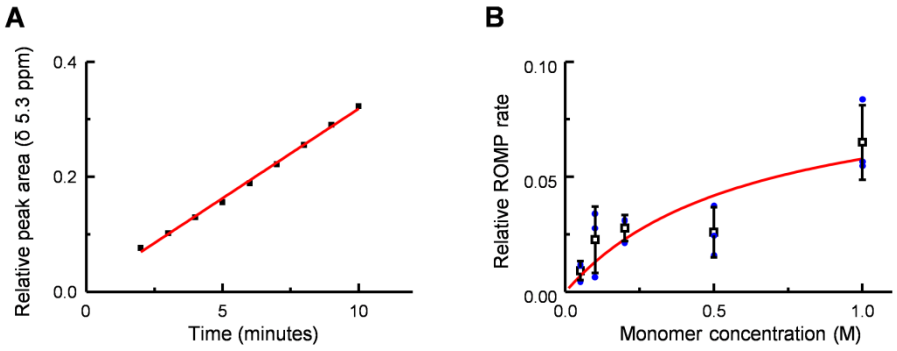

Fig. S37. ^{1}H NMR measurement of the relative ROMP rates catalyzed by G2 (10^{-5} M) vs. norbornene concentrations. (**A**) Formation of polynorbornene in the first 10 minutes at 0.2 M norbornene. Polynorbornene formation was determined the peak area of its proton at δ5.3 ppm (**Fig. S12**) relative to the peak area of TMS (δ 0.0 ppm). The slope of a linear fit (the red line) was used as the relative ROMP rate. (**B**) Relative ROMP rate exhibited saturation kinetics with increasing norbornene concentration. Red line: saturation curve fit, giving an effective dissociation constant of norbornene of ~0.62 M. Blue dots: relative rates from three independent measurements for every monomer concentration; black squares: averages of blue dots for every monomer concentration; error bar is s.d.

5.7.5. Additional experimental results on polydispersity of polymers in real-time growth trajectories.

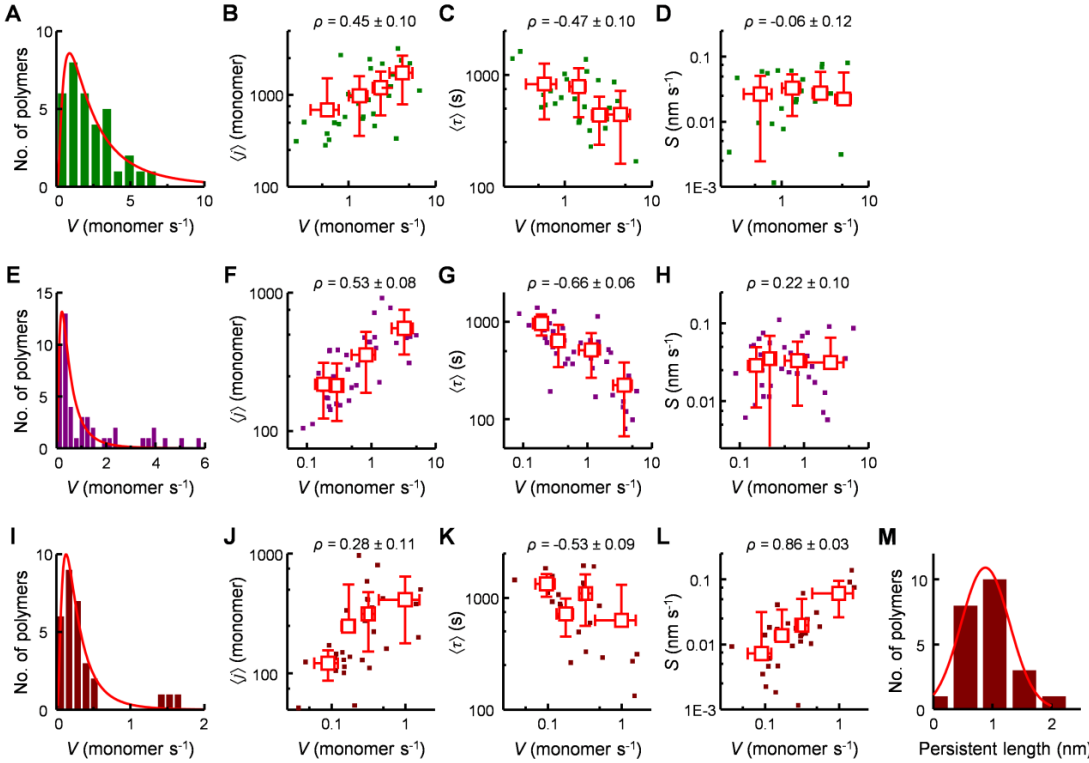

Fig. S38. Origin of dispersion among individual polymers. (**A-D**) Histogram of the average polymerization rate V of individual polymers grown under 1 M norbornene and 4.5 pN force (**A**), and correlation plots between the average polymerization rate V of each polymer molecule and its average jump length (**B**), average waiting time (**C**), and average slope of the waiting periods (**D**), with the respective Pearson's correlation coefficients. (**E-H**) Same as A-D but for 0.1 M norbornene and 17 pN force. (**I-L**) Same as A-D, but for 1 M *cis*-cyclooctene and 17 pN force. (**M**) Distribution of the persistence length p of single polycyclooctene molecules; red line: Gaussian fit centered at 0.88 ± 0.12 nm.

For homopolymers, the polydispersity index *Đ* can be expressed by degree of polymerization (*67*):

$$Đ = \frac{X_w}{X_n} \qquad \textbf{Eqn. S14}$$

where X_w is the weight-averaged degree of polymerization, X_n is the number-averaged degree of polymerization. Based on this, Đ of polymers grown under 1 M norbornene, 17 pN force (**Fig. 4A**) is 1.6 ± 0.3.

Đ could also be calculated using the distribution of average polymerization rate. The degree of polymerization X is equal to the product of polymerization rate V and reaction time t (i.e., $X = V \cdot t$). Assuming all polymers were grown over the same period of time t, the polydispersity index Đ can then be expressed as:

$$Đ = \frac{X_w}{X_n} = \frac{V_w t}{V_n t} = \frac{V_w}{V_n} \qquad \textbf{Eqn. S15}$$

where V_w is the weight-averaged polymerization rate, and V_n is the number-averaged polymerization rate. Based on the distribution of averaged polymerization rate V, Đ of polymers grown under 1 M norbornene, 17 pN force is 1.5 ± 0.4.

6. Additional references.

38. Y. Seol, K. C. Neuman, in *Single Molecule Analysis: Methods and Protocols,* E. J. G. Peterman, G. J. L. Wuite, Eds. (Humana Press, Totowa, NJ, 2011), pp. 265-293.

39. J. Lipfert, X. Hao, N. H. Dekker, Quantitative Modeling and Optimization of Magnetic Tweezers. *Biophys. J.* **96**, 5040-5049 (2009).

40. C. Gosse, V. Croquette, Magnetic tweezers: micromanipulation and force measurement at the molecular level. *Biophys. J.* **82**, 3314-3329 (2002).

41. J. Lipfert, J. J. W. Kerssemakers, M. Rojer, N. H. Dekker, A method to track rotational motion for use in single-molecule biophysics. *Rev. Sci. Instrum.* **82**, 103707 (2011).

42. T.-Y. Chen *et al.*, Concentration- and chromosome-organization-dependent regulator unbinding from DNA for transcription regulation in living cells. *Nat. Commun.* **6**, 7445 (2015).

43. T. R. Strick, J.-F. Allemand, D. Bensimon, A. Bensimon, V. Croquette, The Elasticity of a Single Supercoiled DNA Molecule. *Science* **271**, 1835-1837 (1996).

44. S. P. Roberts *et al.*, Magnetically Actuated Single-Walled Carbon Nanotubes. *Nano Lett.* **15**, 5143-5148 (2015).

45. A. J. W. te Velthuis, J. W. J. Kerssemakers, J. Lipfert, N. H. Dekker, Quantitative Guidelines for Force Calibration through Spectral Analysis of Magnetic Tweezers Data. *Biophys. J.* **99**, 1292-1302 (2010).

46. J. F. Marko, E. D. Siggia, Stretching DNA. *Macromolecules* **28**, 8759-8770 (1995).

47. C. Bouchiat *et al.*, Estimating the Persistence Length of a Worm-Like Chain Molecule from Force-Extension Measurements. *Biophys. J.* **76**, 409-413 (1999).

48. C. G. Baumann, S. B. Smith, V. A. Bloomfield, C. Bustamante, Ionic effects on the elasticity of single DNA molecules. *Proc. Natl. Acad. Sci. USA* **94**,

6185-6190 (1997).

49. L.-B. W. Lee, R. A. Register, Hydrogenated ring-opened polynorbornene: A highly crystalline atactic polymer. *Macromolecules* **38**, 1216-1222 (2005).

50. C. D. Wick, M. G. Martin, J. I. Siepmann, Transferable potentials for phase equilibria. 4. United-atom description of linear and branched alkenes and alkylbenzenes. *J. Phys. Chem. B* **104**, 8008-8016 (2000).

51. W. Stöber, A. Fink, E. Bohn, Controlled growth of monodisperse silica spheres in the micron size range. *J. Colloid Interface Sci.* **26**, 62-69 (1968).

52. X. Bantreil, S. P. Nolan, Synthesis of N-heterocyclic carbine ligands and derived ruthenium olefin metathesis catalysts. *Nat. Protocols* **6**, 69-77 (2011).

53. K. Weigl, Technische Universität Kaiserslautern (2006).

54. A. Monge-Marcet, R. Pleixats, X. Cattoen, M. Wong Chi Man, Sol-gel immobilized Hoveyda-Grubbs complex through the NHC ligand: A recyclable metathesis catalyst. *J. Mol. Catal. A: Chem.* **357**, 59-66 (2012).

55. J. P. Jordan, R. H. Grubbs, Small-molecule N-heterocyclic-carbene-containing olefin-metathesis catalysts for use in water. *Angew. Chem. Int. Ed.* **46**, 5152-5155 (2007).

56. J. Elbert *et al*., Reversible activity modulation of surface-attached Grubbs second generation type catalysts using redox-responsive polymers. *Macromolecules* **46**, 4255-4267 (2013).

57. F. Grisi, A. Mariconda, C. Costabile, V. Bertolasi, P. Longo, Influence of *syn* and *anti* configurations of NHC backbone on Ru-catalyzed olefin metathesis. *Organometallics* **28**, 4988-4995 (2009).

58. S. H. Chung, R. A. Kennedy, Forward-backward non-linear filtering technique for extracting small biological signals from noise. *J. Neurosci. Methods* **40**, 71-86 (1991).

59. M. S. Sanford, J. A. Love, R. H. Grubbs, Mechanism and activity of ruthenium olefin metathesis catalysts. *J. Am. Chem. Soc.* **123**, 6543-6554 (2001).

60. J. D. Ng *et al*., Single-molecule investigation of initiation dynamics of an organometallic catalyst. *J. Am. Chem. Soc.* **138**, 3876-3883 (2016).

61. M. G. Martin, J. I. Siepmann, Transferable potentials for phase equilibria. 1. United-atom description of n-alkanes. *J. Phys. Chem. B* **102**, 2569-2577 (1998).

62. J. M. Stubbs, J. J. Potoff, J. I. Siepmann, Transferable potentials for phase equilibria. 6. United-atom description for ethers, glycols, ketones, and aldehydes. *J. Phys. Chem. B* **108**, 17596-17605 (2004).

63. W. Paul, D. Y. Yoon, G. D. Smith, An optimized united atom model for simulations of polymethylene melts. *J. Chem. Phys*. **103**, 1702-1709 (1995).

64. J. P. Bishop, R. A. Register, The crystal–crystal transition in hydrogenated ring-opened polynorbornenes: tacticity, crystal thickening, and alignment. *J. Polym. Sci., Part B: Polym. Phys.* **49**, 68–79 (2011).

65. S. Plimpton, Fast parallel algorithms for short-range molecular dynamics. *J. comput. phys.* **117**, 1–19 (1995).

66. K. Binder. (Oxford University Press, 1995), pp. 179-182.

67. W. Mormann, Polymer education – a matter at the heart of the iupac polymer division. *Macromolecular Symposia* **355**, 8-12 (2015).